

REPORT DOCUMENTATION PAGE

AFRL-SR-AR-TR-04-

Public reporting burden for this collection of information is estimated to average 1 hour per response, including gathering and maintaining the data needed, and completing and reviewing the collection of information. Send collection of information, including suggestions for reducing this burden, to Washington Headquarters Service, Paperwork Reduction Project (0704-0188), Washington, DC 20503.

ces,
this
erson

1. AGENCY USE ONLY (Leave blank)		2. REPORT DATE	3. REPORT TYPE AND DATES COVERED 01 May 2001 - 31 May 2004 FINAL
4. TITLE AND SUBTITLE Optical Coherence Tomographic Imaging and Delivery for Surgical Guidance			5. FUNDING NUMBERS 62227D 0483/01
6. AUTHOR(S) Dr Fujimoto			
7. PERFORMING ORGANIZATION NAME(S) AND ADDRESS(ES) MASSACHUSETTS INST OF TECHNOLOGY OSP BLDG E19-750 77 MASSACHUSETTS AVE CAMBRIDGE MA 02139			8. PERFORMING ORGANIZATION REPORT NUMBER
9. SPONSORING/MONITORING AGENCY NAME(S) AND ADDRESS(ES) AFOSR/NE 4015 WILSON BLVD SUITE 713 ARLINGTON VA 22203			10. SPONSORING/MONITORING AGENCY REPORT NUMBER F49620-01-1-0186
11. SUPPLEMENTARY NOTES			
12a. DISTRIBUTION AVAILABILITY STATEMENT DISTRIBUTION STATEMENT A: Unlimited			12b. DISTRIBUTION CODE
13. ABSTRACT (Maximum 200 words) OCT is an emerging diagnostic imaging technology which was developed by our research group in part under this program. OCT generates cross-sectional images of tissue microstructure with micron scale (1-15 um) resolution by measuring the echo time delay and magnitude of backscattered light. OCT can thus function as a type of "optical biopsy," enabling imaging of tissue with resolution approaching conventional biopsy and histopathology, but without the need to remove and process specimens. Over the three years of work under this contract, we have made significant progress in a number of areas: development of new laser technology for ultrahigh resolution imaging; new technology and measurement techniques for OCT imaging; in vitro imaging studies to establish the feasibility of using OCT for optical biopsy; and preliminary clinical studies. These key advances are summarized in sections entitled: A. Ultrahigh Resolution Technology for OCT imaging B. Optical Biopsy and Novel Devices for Clinical Applications C. Clinical Imaging using Optical Coherence Tomography			
14. SUBJECT TERMS			15. NUMBER OF PAGES
			16. PRICE CODE
17. SECURITY CLASSIFICATION OF REPORT Unclassified	18. SECURITY CLASSIFICATION OF THIS PAGE Unclassified	19. SECURITY CLASSIFICATION OF ABSTRACT Unclassified	20. LIMITATION OF ABSTRACT UL

FINAL REPORT

Air Force Office of Scientific Research
Contract No. F49620-01-1-0186

1 May 2001 - 31 May 2004

Optical Coherence Tomographic Imaging
and Delivery For Surgical Guidance

Principal Investigator

Prof. James G. Fujimoto
Department of Electrical Engineering and Computer Science
and Research Laboratory of Electronics
Massachusetts Institute of Technology
77 Massachusetts Avenue
Cambridge, MA 02139

20041230 011

Air Force Office of Scientific Research

FINAL REPORT GRANT #: F49620-01-1-0186
P.I.: Dr. James G. Fujimoto
INSTITUTION: Massachusetts Institute of Technology
GRANT TITLE: Optical Coherence Tomography Imaging and Delivery for
 Surgical Guidance
AWARD PERIOD: 1 May 2001 - 31 May 2004

Objective of the Proposal

The objective of this program is to develop and apply optical coherence tomography (OCT) for biomedical applications. OCT is an emerging technology for performing in situ, real time cross-sectional imaging of tissue microstructure.

Accomplishments

OCT is an emerging diagnostic imaging technology which was developed by our research group in part under this program. OCT generates cross-sectional images of tissue microstructure with micron scale (1-15 μm) resolution by measuring the echo time delay and magnitude of backscattered light. OCT can thus function as a type of "optical biopsy," enabling imaging of tissue with resolution approaching conventional biopsy and histopathology, but without the need to remove and process specimens. Over the three years of work under this contract, we have made significant progress in a number of areas: development of new laser technology for ultrahigh resolution imaging; new technology and measurement techniques for OCT imaging; in vitro imaging studies to establish the feasibility of using OCT for optical biopsy; and preliminary clinical studies.

These key advances are summarized in sections entitled:

- A. Ultrahigh Resolution Technology for OCT imaging
- B. Optical Biopsy and Novel Devices for Clinical Applications
- C. Clinical Imaging using Optical Coherence Tomography

A list of publications supported under this contract is appended at the end.

Ultrahigh Resolution Technology for OCT imaging

Optical coherence tomography (OCT) is an emerging medical imaging technology, developed by our research group in 1991 [1], which is promising for applications in several medical fields [2]. OCT enables the visualization of tissue microstructure *in situ* and in real time with resolutions in the 1-10 μm range. OCT is a promising technique for optical biopsy, enabling the visualization of tissue pathology [3-6]. Enhancing the axial resolution of OCT has been a major focus of the previous research. Clinical OCT systems often use superluminescent diodes (SLDs) that enable imaging with 10-15 μm axial resolution. These resolutions are typically insufficient for many

applications such as identifying neoplastic changes for cancer detection or tissue morphological and structural features for the visualization of other pathologies.

Over the three years of work under this contract, we have made significant progress in developing OCT technology to achieve ultrahigh resolution imaging. In addition, we have made advances in optical coherence microscopy techniques which promise to enable *in vivo* cellular-level imaging. The use of broadband laser sources for ultrahigh resolution OCT imaging has also enabled the development of spectroscopic methods for enhancing contrast in OCT images. Finally, this section will describe studies in ultrahigh resolution spectral domain OCT, which enables over an order of magnitude improvement in imaging speed for *in vivo* ultrahigh resolution OCT imaging.

Ultrahigh Resolution OCT Imaging using Microstructure Fibers

The longitudinal resolution in OCT images is inversely proportional to the optical bandwidth and proportional to the square of the center wavelength of the light source. Ultrahigh resolution OCT requires extremely broad bandwidths because of this $\lambda^2/\Delta\lambda$ dependence of the longitudinal resolution. This is particularly the case for the spectral region between 1.2 μm and 1.5 μm . This spectral region is important for OCT because of the high penetration depth in biological tissue and the possibility to perform spectral resolved imaging of water absorption bands. Superluminescent diodes are used in conventional OCT systems and typically yield 10-15 μm longitudinal resolutions. We demonstrated previously OCT imaging with resolutions of 1 μm at 800 nm [7] and 5.1 μm at 1300 nm [8] in biological tissue using a Kerr-lens modelocked Ti:Sapphire laser with double-chirped mirrors and the self phase modulation broadened spectrum of a Kerr-lens modelocked Cr:Forsterite laser, respectively.

These broadband Kerr-lens modelocked lasers are not available commercially and require double chirped mirrors. We investigated a broad band light source based on a standard pulse duration Ti:Sapphire laser using continuum generation in air-silica microstructured fibers. High nonlinearity, air-silica microstructure fibers [9] or tapered fibers [10] can generate an extremely broadband continuum using low energy femtosecond pulses. These fibers achieve high nonlinearities by using a tight mode confinement and shifting the zero of dispersion to shorter wavelengths. We achieved a free-space axial resolution of 2.5 μm at a 1.3 μm center wavelength and demonstrated the application of the OCT system for *in vivo* imaging of biological tissue [11]. Figure 1 (left) shows a schematic of the experimental setup. We launched 100 fs pulses generated by a commercial Kerr-lens modelocked Ti:Sapphire laser, which was pumped by a frequency doubled Nd:Vanadate laser into a 1 m length of microstructure fiber. The fiber continuum was collimated with a microscope objective (MO), spectrally filtered by a long-pass filter and focussed with a chromatically corrected custom-designed lens (AL) into a dispersion shifted single mode fiber. A custom-designed lens and broadband 3dB fiber couplers (FC), designed for 1300 nm center wavelength (FC), were used in the OCT setup. Since the light source had excess amplitude noise, a dual balanced detection with two InGaAs photodiodes (D1, D2) was used. Polarization controllers (PC) minimized the polarization mismatch of the interferometer arms to avoid degradation of the shape and the peak height of the interference fringes.

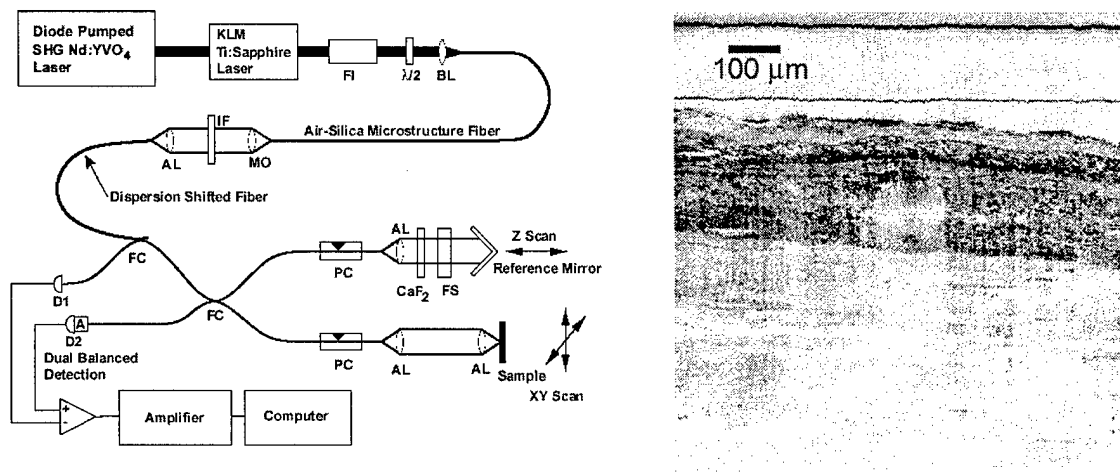


Figure 1. (left) Ultrahigh resolution OCT system using continuum generation in an air-silica microstructure fiber as the light source. See text for explanation of the acronyms. (right) *In vivo* ultrahigh resolution ($\sim 6 \times 2.5 \mu\text{m}$, transverse \times axial resolution, $1.0 \times 1.0 \text{ mm}$; 1000×3000 pixels) OCT image of a hamster cheek pouch showing the epithelium, muscular layers, and a blood vessel.

The feasibility of *in vivo* ultra high resolution imaging using this source was demonstrated by imaging the cheek pouch of a Syrian hamster, a well-established animal model for studies of cancer progression. Figure 1 (right) is an *in vivo* image of cheek pouch which shows the epithelium, connective tissue, muscular layers, and a blood vessel at ultrahigh resolution. In conclusion, we successfully demonstrated the use of continuum generation in an air-silica microstructure fiber for OCT imaging [11]. We achieved a free-space axial resolution of $2.5 \mu\text{m}$ at a $1.3 \mu\text{m}$ center wavelength and demonstrated the application of this ultrahigh resolution OCT system for *in vivo* imaging of biological tissue.

Compact Ultrahigh Resolution System for Real-Time *In vivo* Imaging

One of the key problems in OCT has been the lack of compact, high performance, low coherence light sources with sufficient bandwidth and power to enable high resolution, real time imaging. Compact, diode pumped solid state lasers can generate femtosecond pulses, but do not have sufficient bandwidths for high resolution imaging. We recently demonstrated ultrahigh resolution OCT with an axial resolution of $2.5 \mu\text{m}$ at 1300 nm center wavelength using continuum generation with femtosecond pulses from a Ti:Sapphire laser coupled into an air-silica microstructure fiber. While this approach achieves high resolutions in the important 1300 nm wavelength range, the Ti:Sapphire laser requires a high power pump laser which makes the light source expensive and bulky.

Working in collaboration with investigators from HighQ Laser Productions in Austria, we developed a compact ultrahigh resolution OCT system based on new broadband light sources that can emit in either the $1 \mu\text{m}$ and $1.3 \mu\text{m}$ wavelength range. The 1300 nm wavelength allows

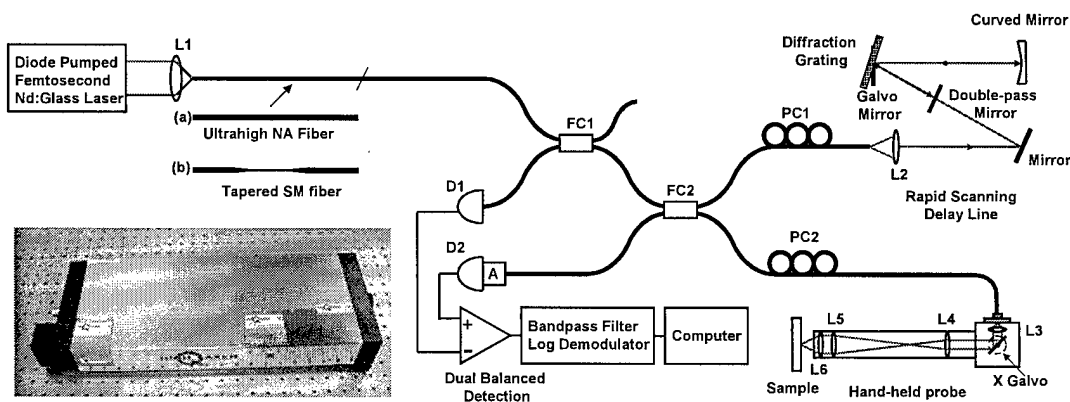


Figure 2. Schematic of the OCT system using a femtosecond diode pumped Nd:Glass laser (bottom left corner) with continuum generation either (a) in an ultrahigh numerical aperture single mode fiber or (b) in a tapered single mode fiber.

good image penetration depth in tissue, while the 1064 nm wavelength offers a good compromise high axial resolution, but lower penetration depths. The laser and OCT system are compact, robust, transportable and well suited for clinical studies.

Figure 2 shows a schematic of the experimental setup. A compact diode pumped femtosecond Nd:Glass laser (HighQ Laser Productions) generates pulses with 110-150 fs duration, 150 mW average power at 75 MHz repetition rate and 1064 nm wavelength. Either an ultrahigh numerical aperture fiber or a tapered fiber can be used to generate a spectrum centered at 1 μm or 1.3 μm wavelength, respectively. The OCT system consists of broadband 3 dB fiber couplers (FC), and custom designed achromatic lenses (L). In order to accommodate the broad bandwidths and enable real time imaging, delay scanning is performed using a rapid scanning delay line with reflective optics. A hand-held probe was developed for *in vivo* imaging. An x-galvo is used for transverse scanning at 4 frames per second. Dispersion is matched in the two arms of the interferometer in order to maintain resolution. Dual balanced detection with two photodiodes (D1, D2) is used to cancel the intensity noise of the light source. Polarization controllers (PC1, PC2) are used in the sample arm and the reference arms.

To demonstrate the performance of the system in an *in vivo* imaging application, an African frog tadpole (*Xenopus laevis*) was imaged (Fig. 3). The continuum light sources yield an axial resolution of 5-6 μm in air or $\sim 4 \mu\text{m}$ in biological tissue, which is three times higher than with the conventional semiconductor sources (superluminescent diodes or amplified spontaneous emission light sources). This improved resolution enables the differentiation of small features, which cannot be resolved using conventional light sources.

In vivo ultrahigh resolution OCT imaging of the hamster cheek pouch was also demonstrated at 1 μm (Fig. 4a). We chose this tissue it has a morphology consisting of thin layers than can only be well resolved by using an ultrahigh resolution system. Fig. 4b shows an image of human skin, also acquired *in vivo* and at high speed. The stratum corneum is easily visible. Features such as

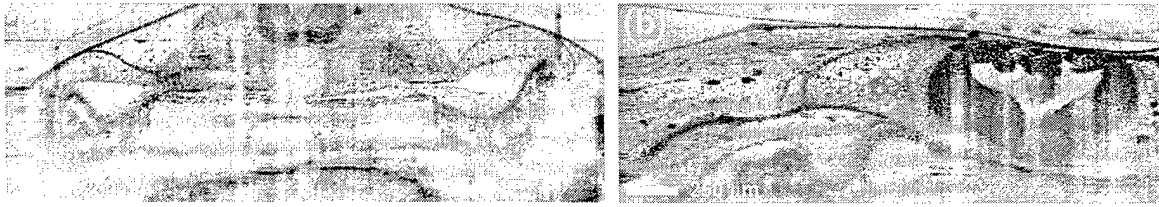


Figure 3. *In vivo* OCT images of an African frog tadpole (*Xenopus laevis*) (a) at 1064 nm using spectral broadening in a high NA fiber (b) at 1300 nm using continuum generation in a tapered fiber. The axial resolution is 5-6 μm in both cases.

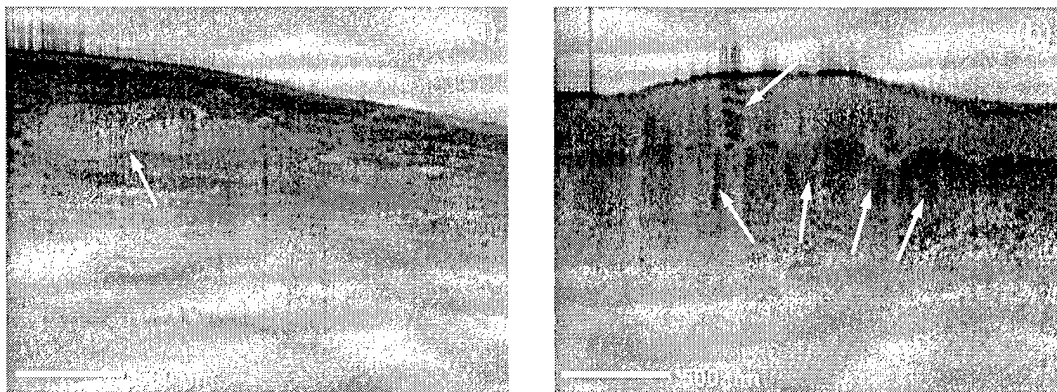


Figure 4. *In vivo* OCT images acquired at 4 frames per second with the 1 μm light source. The axial and transverse resolution are 5.5 μm and 11 μm , respectively. (a) Image of a hamster cheek pouch. The junction of 2 blood vessels is visible. (b) Image of human skin. Sweat ducts and the junction between the epidermis and the dermis can be resolved.

sweat ducts and the dermal-epidermal junction can also be differentiated. The images are 2 mm x 1.6 mm (transverse x axial) in size and contain 500 x 360 pixels.

These results demonstrate the utility of our system to perform *in vivo* ultrahigh resolution OCT imaging with a portable light source based on the generation of supercontinuum by nonlinear effects in optical fibers. Such system, with its user-friendly laser, opens the door to the ultrahigh resolution OCT imaging in the clinic, and will be a powerful tool for future studies.

All-Fiber Continuous-Wave (CW) Raman Continuum Light Source for High Resolution OCT

The lack of compact and portable high-performance broadband light sources with sufficient power and bandwidths has been a limitation to achieving ultrahigh resolution, high speed OCT imaging outside the laboratory setting. Femtosecond solid-state lasers can directly generate broad bandwidths for OCT imaging, but are difficult to operate outside the laboratory [7, 12]. Nonlinear and microstructure fibers pumped by femtosecond bulk and fiber systems have also enabled imaging with unprecedented resolutions, but require the use of femtosecond lasers [11,

13, 14]. Reductions in cost can be achieved by using low-threshold femtosecond lasers, which use inexpensive low-power pump lasers [15, 16]. The 1300 nm wavelength region is of particular interest for biomedical applications because it permits improved imaging depth when compared to shorter wavelengths due to reduced scattering [17]. The development of broadband light sources for OCT, therefore, focused on this wavelength range [11, 14, 18, 19]. Recent work has also investigated light source development and imaging at center wavelengths closer to 1000 nm, which provide a compromise of higher resolution for a given bandwidth at the expense of reduced image penetration [14, 20].

A novel approach to broadband continuum generation in photonic crystal fibers has become possible due to the development of high-power, all-fiber pump sources. These new light sources promise ultrahigh resolution, high speed OCT imaging with lower cost and complexity than what is possible with femtosecond laser-based light sources. Microstructure and photonic crystal fibers typically have been pumped with femtosecond lasers in order to provide the peak powers necessary to initiate self-phase modulation and four-wave-mixing-supported continuum generation under conditions of anomalous or near-zero dispersion. However, the use of high intensity femtosecond sources for continuum generation in holey fibers leads to severe spectral modulation of the continuum in the vicinity of the pump wavelength. This spectral modulation produces side lobes and reduced contrast in the interferometric point spread function. Femtosecond quasi-CW-pulsed pumping of holey fibers also may result in excessive temporal instability of the continuum and nonlinearly amplified quantum noise, which can lead to dramatic relative intensity noise fluctuations [21]. An alternative to using high peak powers is to increase the effective nonlinear interaction length of the Raman interaction, using longer pump pulses which reduces dispersive walk-off. Stimulated Raman scattering is the principle nonlinearity for continuum generation by using nanosecond-scale pump pulses [22, 23]. Recently, the possibility of low peak power and even continuous-wave, multiwatt Raman continuum generation in highly nonlinear fibers was demonstrated [24]. Continuous-wave pumping of nonlinear fibers can enable the development of robust and turnkey continuum light sources that require no optical alignment, thus enabling high speed, ultrahigh resolution OCT imaging in a wide range of applications outside the laboratory.

In collaboration with Professor James R. Taylor's group at Imperial College, we have demonstrated a continuous-wave-pumped, all-fiber Raman continuum light source with 330 mW power for high speed, ultrahigh resolution OCT imaging in scattering tissue. This light source is robust, compact, turnkey, and suitable for clinical applications. The broadband fiber light source was based on a 10 W continuous-wave, nonpolarized, multimode diode-pumped, single-mode Yb-fiber laser (IPG Photonics) directly spliced to an anomalously dispersive holey fiber (Crystal Fiber). The Raman-soliton continuum had 5.5 W of total power and a spectral width of 318 nm (at 20 dB). The spectral range from 1090 to 1370 nm was flat to ± 5 dB and contained 2.3 W of power. The output was filtered using a special wavelength division multiplex (WDM) coupler to remove the pump wavelength. Figure 5 shows the continuum produced by the Raman continuum source, and typical spectra before and after spectral shaping by the WDM coupler. The output power after the coupler was ~ 330 mW and the spectrum was Gaussian-shaped with a bandwidth of ~ 140 nm, which corresponds to a theoretical resolution of $5 \mu\text{m}$ in free space. The complete light source contains no bulk optical components, requires no alignment, and is turnkey, compact (25 x 25 x 20 cm) and robust.

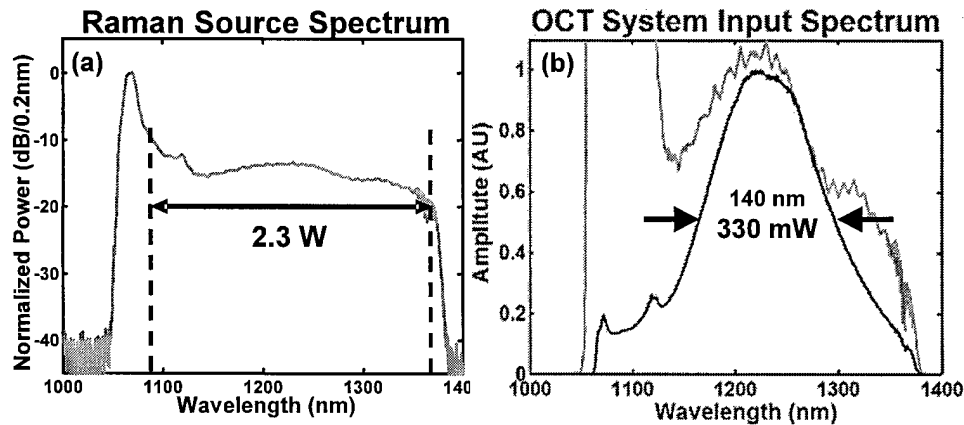


Figure 5. (a) Continuum produced by continuous wave, Raman light source. (b) Typical output spectrum before and after spectral shaping.

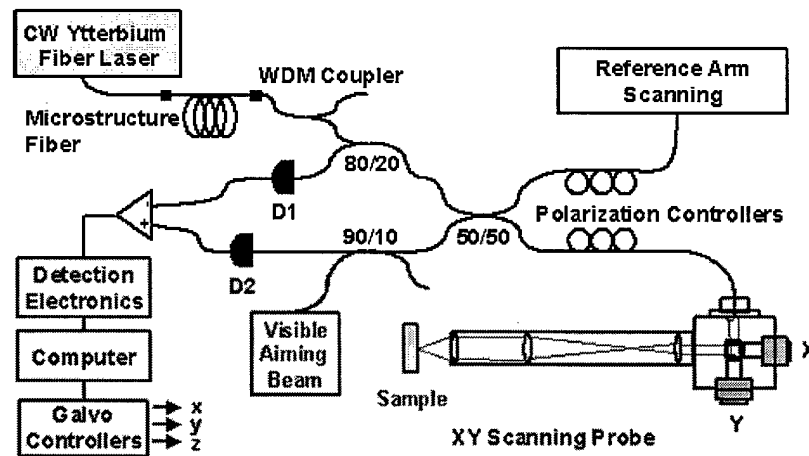


Figure 6. Schematic of a high speed, ultrahigh resolution OCT system using an all-fiber Raman continuum light source. The system uses broadband 80/20 and 50/50 couplers to optimize the power on the sample and is coupled back to the detectors. Dispersion was matched in the sample and reference arms of the interferometer in order to maintain high axial resolution.

Figure 6 shows the schematic of the experimental setup. The OCT system consists of broadband 80/20 and 50/50 fiber couplers to optimize power coupled back to the detectors. The reference arm was scanned using a reflective delay scanner. Polarization controllers were used in both the sample arm and the reference arms. *In vivo* imaging was performed using an X-Y galvanometer scanning probe. Near-infrared achromatic lenses were used to minimize chromatic aberration. Dual-balanced detection with two InGaAs photodiodes was used to reduce excess intensity noise. The interference signal was electronically band-pass filtered, logarithmically demodulated, low-pass filtered, and digitized. The performance of the OCT system using the Raman continuum light source was measured by using an isolated reflection from a single



Figure 7. High speed, ultrahigh resolution *in vivo* OCT image of a Syrian hamster cheek pouch. The epithelial layer (e), muscular layers (m), and two prominent vessels (v) are clearly visible. A microscope cover glass (c) was placed over the top of the cheek pouch ($\sim 18 \mu\text{m} \times 4.8 \mu\text{m}$ transverse \times axial resolution, 500×1000 pixels, $2.5 \times 1.8 \text{ mm}$).

mirror. To maintain axial resolution, the dispersion in the interferometer sample and reference arms was carefully matched. The measured axial resolution was $6.3 \mu\text{m}$ in air, which corresponds to $4.8 \mu\text{m}$ in tissue. The detected optical spectrum was measured to be 110 nm by Fourier transformation of the interferometric signal. This reduction in bandwidth may be the result of wavelength dependence of the fiber couplers, as well as wavelength variations in the sensitivity of the InGaAs photodiodes.

We demonstrated high speed, ultrahigh resolution *in vivo* OCT imaging in the hamster cheek pouch, which is a well-established model for studies of cancer progression. To minimize the effect of wavefront aberration and dehydration, and to achieve better index matching, the cheek pouch was irrigated with saline and covered with a thin cover glass. Figure 7 shows a high speed, ultrahigh resolution *in vivo* image of the hamster cheek pouch with $<5 \mu\text{m}$ axial resolution. The image had 500 transverse pixels and 1000 axial pixels, and it measured 2.5 mm by 1.8 mm . The axial dimension was scaled by 1.3 to account for the approximate index of refraction. The epithelial layer, muscular layers, and two prominent vessels are clearly visible in the hamster cheek pouch.

In conclusion, we demonstrated an all-fiber, continuous-wave-pumped, broadband Raman continuum fiber light source at a center wavelength of $\sim 1.3 \mu\text{m}$ for high speed, ultrahigh resolution *in vivo* OCT imaging. We achieved an axial resolution of $<5 \mu\text{m}$ in tissue, which is a factor of 2-3 times finer than what is possible using conventional superluminescent diode light sources. This fiber Raman light source requires no alignment; it is compact, turnkey, and promising for clinical OCT imaging applications. Broader output spectra and lower excess noise may be obtained using higher power Yb lasers and different fiber geometries. Although the cost of the light source is rather high, because of the cost of the photonic crystal fiber, these fibers are expected to be available at significantly lower cost in the future. The future cost should be

significantly lower than that of bulk solid-state femtosecond laser-based light sources. The high performance and ease of use of this light source promises high speed, ultrahigh resolution OCT imaging in a wide range of applications.

Real-Time High Resolution OCT using All-Fiber Femtosecond Fiber Laser Continuum at 1.5 μm

Compact, broad bandwidth supercontinuum sources were recently demonstrated by using femtosecond fiber lasers in combination with nonlinear fibers [25, 26]. Fiber lasers can provide a more compact and robust approach for ultrahigh resolution imaging when compared to bulk solid-state lasers. Fiber-based light sources have achieved sub-2- μm high-resolution OCT in the 1300 nm wavelength region [19]. Because the optical scattering in tissues is reduced and the penetration depth is increased at longer wavelengths, the wavelength region around 1.4-1.6 μm is of interest for OCT imaging [17, 27]. This wavelength region is also attractive for the characterization of optical devices or for spectroscopic applications using water absorption [28].

We developed an all-fiber scheme for real-time high-resolution OCT imaging in the 1.4-1.7 μm wavelength region. A low-noise supercontinuum with 38 mW power and 180 nm bandwidth was generated using a high-power, stretched-pulse, passively modelocked fiber laser and highly nonlinear fiber. *In vivo* imaging of human skin is demonstrated using the SC source and a high-speed OCT imaging system.

Figure 8 shows the experimental setup of OCT imaging using the high-power stretched-pulse passively modelocked Er-doped fiber laser. The generated supercontinuum was coupled into a high-speed OCT system. The OCT system consists of an optical circulator and a broadband 50/50 fiber coupler to optimize power coupled back to the detectors. The reference arm was scanned using a reflective scanner with a scan speed of 7.6 m/s and a repetition rate of 1900 Hz. Polarization controllers were used in both the sample arm and the reference arm to match the polarizations in the two interferometer arms. *In vivo* imaging was performed using an XY galvanometer scanning probe. A dual-balanced detection configuration was performed with two InGaAs photodiodes. The detected interference signal was band-pass filtered, logarithmically demodulated, low-pass filtered, and acquired by the computer.

The performance of the OCT system was measured by using an attenuated isolated reflection. To maintain high axial resolution, the dispersion in the two arms of the interferometer was carefully matched. Figures 9(a) and 9(b) show the interference signal and the logarithmic demodulated signal after band-pass and low-pass filtering. Since the spectral shape is almost Gaussian, the magnitude of side lobes was small on a linear scale. On a log scale, there are several small side lobes at -40 to -50 dB below the main peak, which is caused by small residual modulation in the spectrum. The measured axial resolution was 7.4 μm full-width-at-half-maximum (FWHM) in air, which corresponds to 5.6 μm in tissue. The detected optical spectrum was measured to be 151 nm by Fourier transforming the interferometric signal. This reduction in bandwidth may be due to the wavelength dependence of the circulator, couplers, and optical lenses, as well as wavelength variations in the sensitivity of the InGaAs photodiodes. The system sensitivity was 98.7 dB with a power of 12 mW incident on the sample. This sensitivity is near the theoretical sensitivity for this incident power and detection bandwidth.

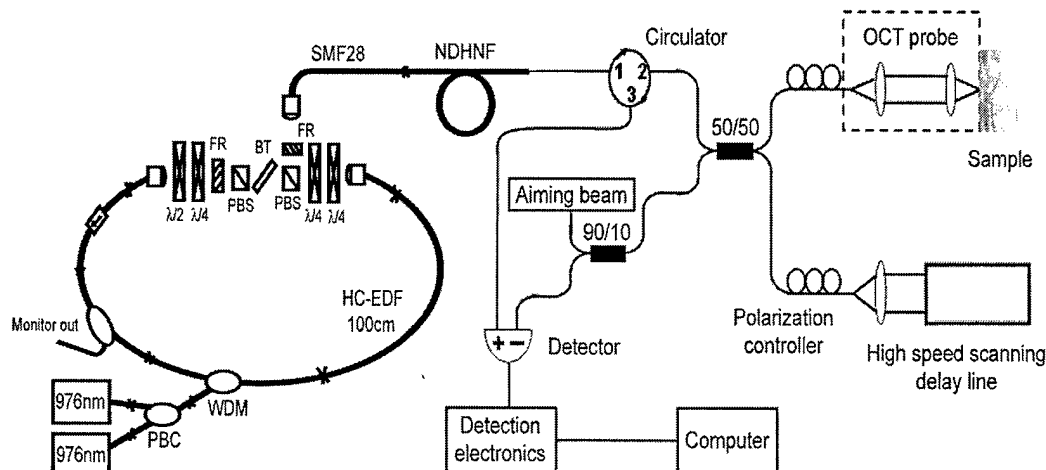


Figure 8. Schematic of an all fiber, real-time, ultrahigh resolution OCT system at $1.55 \mu\text{m}$ wavelength. (PBC: polarization beam combiner; WDM: wavelength division multiplexed coupler; HC-EDF: high concentration Er doped fiber; PBS: polarization beam splitter; FR: Faraday rotator; BT: birefringent plate).

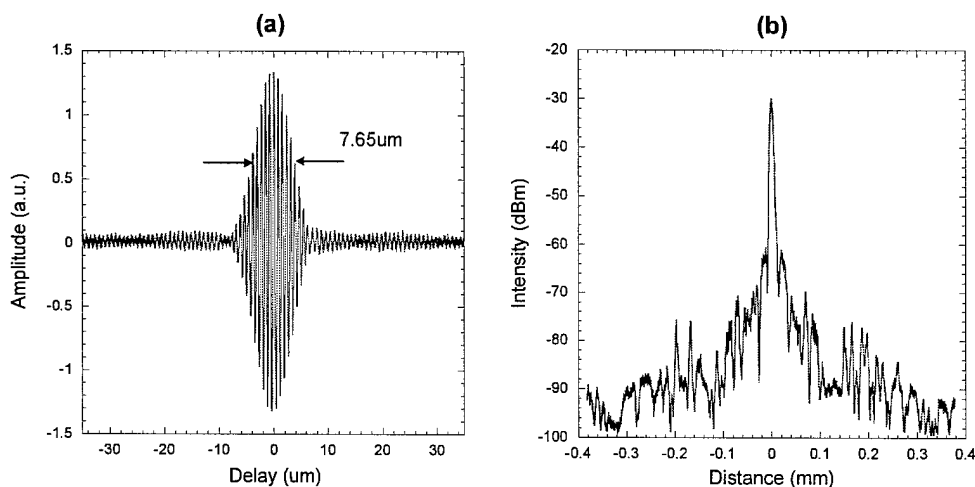


Figure 9. (a) Interference signal point spread function and (b) logarithmically demodulated signal showing an axial resolution of $7.4 \mu\text{m}$ in air, which corresponds to $5.6 \mu\text{m}$ in tissue.

We demonstrated the feasibility of using this light source for high-speed *in vivo* OCT by imaging the human skin. To minimize the effect of wavefront aberration, and tissue dehydration, and to achieve better index matching, a transparent gel was applied. Figure 10 shows an *in vivo* image of human skin. The image consists of 500 transverse scans with 1000 pixels per scan, which covers an area of 2.5 mm by 1.8 mm . The image was scaled by 1.3 times in the axial dimension in order to compensate for the approximate index of refraction. The epidermis, sweat duct, and junction of epidermis and dermis are clearly visible.

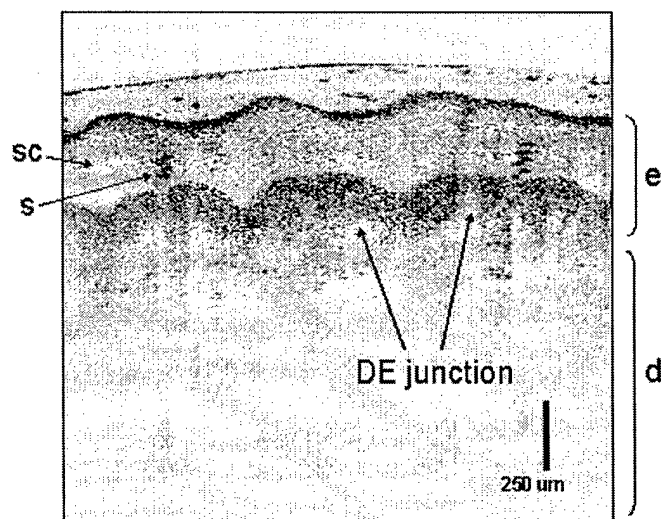


Figure 10. High-speed *in vivo* OCT image of human skin. The stratum corneum (sc), epidermis (e), sweat duct (s), and dermis (d) are clearly visible ($\sim 18 \mu\text{m} \times 4.8 \mu\text{m}$ transverse \times axial resolution; 500 \times 1000 pixels; 2.5 \times 1.8 mm).

In summary, we demonstrated an all-fiber, real-time, high resolution OCT imaging system by using a high-power, broadband, supercontinuum fiber laser light source in the $1.55 \mu\text{m}$ wavelength region. Fiber lasers can provide a more compact and robust approach to ultrahigh resolution imaging than what is possible with bulk solid-state lasers. Low-noise supercontinua with 180 nm bandwidth and 38 mW output power was generated using a stretched-pulse, passively modelocked high-power femtosecond fiber laser and normal dispersive highly nonlinear fiber. We achieved an axial resolution of $\sim 7.4 \mu\text{m}$ in air and $\sim 5.6 \mu\text{m}$ in tissue at a center wavelength of $\sim 1.5 \mu\text{m}$. This light source is stable, compact, and self-starting, and it should be useful for a wide range of high resolution high-speed OCT imaging applications.

Compact Cr^{4+} :Forsterite Laser for High Resolution Endoscopic OCT Imaging

One of the medical areas where high resolution OCT imaging could significantly impact the detection and diagnosis of disease is endoscopic imaging [29]. Gastrointestinal (GI) endoscopy has received increased attention due to the prevalence of esophageal, stomach, and colonic cancers. In the early stages of development, these cancers manifest as cellular and architectural changes in the epithelium or mucosal layers located inside the wall of the gastrointestinal tract. In contrast to conventional video endoscopy, which can only visualize the surface alterations, OCT can detect changes in tissue morphology beneath the tissue surface. Therefore, endoscopic imaging with high resolution OCT could potentially improve the detection, visualization, and diagnosis of gastrointestinal diseases.

Previous studies of endoscopic OCT imaging have documented the capability of OCT to differentiate abnormal GI pathologies such as the Barrett's esophagus, adenomatous polyps, and adenocarcinoma from normal tissues [30-36], while the resolution of these previous OCT

systems is typically 10-15 μm . Higher resolution OCT systems may enable the identification of early neoplastic changes in gastrointestinal tissue. This advance could enable image-guided biopsy at high resolution, with the prospect of improving the sensitivity of biopsy by reducing false-negative rates caused by sampling errors.

In this study, we have developed high resolution endoscopic OCT imaging system by using a compact, broadband Cr^{4+} :Forsterite laser as the light source. Prismless operation within the laser cavity was achieved by using double-chirped mirrors for intracavity dispersion compensation [37]. Combined with a dispersion-shifted highly non-linear fiber, a spectral bandwidth of >200 nm at center wavelength of 1250 nm and an output power of 50 mW was generated, as shown in Figure 11. The compact Cr^{4+} :Forsterite laser has a footprint of 40 cm by 60 cm, and its portability makes it accessible to clinical settings.

Figure 12 depicts the schematic of the OCT imaging system. Light was coupled into a broadband optical circulator and a 90/10 fiber optic coupler, which transmits 90% of the incident light to the sample arm. A rapid scanning delay line in the reference arm provided real-time imaging up to 3125 axial scans per second. Polarization controllers were used in both the sample and reference arms to optimize signal strength and interference. To match the optical dispersion within the system, SFL6 and LaKN22 dispersion-compensating glass (DCG) was inserted in the reference arm, and an air-gap coupling (AGC) was used in the sample arm. The use of the air coupling allowed precise dispersion compensation and enabled broadband operation for high resolution imaging performance. The OCT signal after interference was split into two orthogonal polarization dependent channels by a polarizing beam splitter (PBS), and the two detector outputs were digitally demodulated. A polarization diversity signal was calculated using the square root of the sum of the squared signal intensities from the two channels. Due to the bandwidth limitations in the optical circulator and other optical components in the sample and reference arms, the back-coupled spectrum on the detector has a bandwidth of 150 nm, which corresponds to a theoretical axial resolution of 4.6 μm in air. The width of the measured axial point spread function is 5 μm , which is a two- to three-fold improvement over standard OCT systems. This corresponds to a 3.6 μm resolution in the tissue, assuming a 1.4 mean index of refraction. With improvements in the bandwidth of the optical components, higher axial resolutions could be achieved.

The light was delivered through a 1.5-mm-diameter imaging catheter with a 15 μm focal spot size and a 0.5 mm focal distance from the outer wall of the catheter sheath. The catheter was driven by a magnetic actuator in order to create a linear cross-sectional imaging scan through the tissue surface. A 4 Hz frame rate was implemented in the *in vivo* imaging to reduce the movement artifacts.

The feasibility of endoscopic OCT imaging was demonstrated on an animal model. The gastrointestinal tract of the New Zealand White rabbit was imaged by using the linear scanning catheter. All imaging procedures were performed at MIT facilities with protocols approved by the MIT Committee on Animal Care (CAC). The rabbit was anesthetized, and the OCT imaging catheter was manually introduced into the upper gastrointestinal (esophagus) and lower gastrointestinal (colon) tracts respectively.

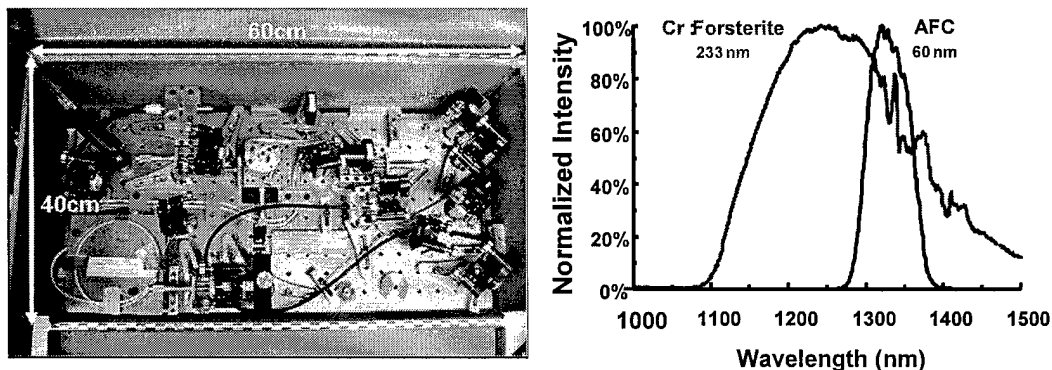


Figure 11. (a) The photo of the compact Cr^{4+} :Forsterite laser with the optical beam highlighted (top: pump light; middle: laser cavity; bottom: output coupling). (b) The output spectrum of the Cr^{4+} :Forsterite laser, compared with the spectrum of standard SLD source.

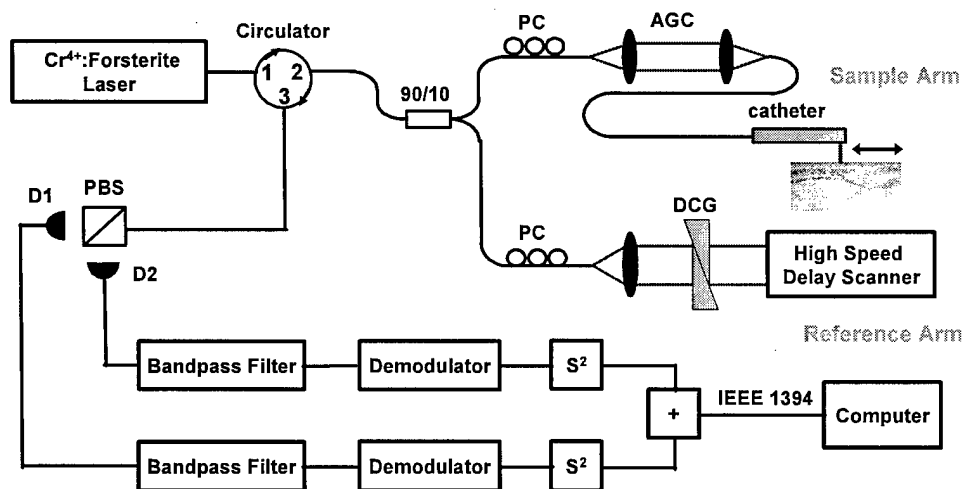


Figure 12. Schematic of an endoscopic OCT imaging system using a broadband Cr^{4+} :Forsterite light source. Accurate dispersion matching is achieved through the use of an air-gap coupling (AGC) and dispersion-compensating prisms (DCG), which enables broadband, high resolution operation.

Figure 13(a) shows an *in vivo* OCT image of the rabbit esophagus taken with the linear scanning catheter. The corresponding histology is shown in Figure 13(b). The structure of the esophagus is delineated clearly, with well-organized layers of the squamous epithelium (ep), lamina propria (lp), muscularis mucosa (mm), submucosa (sm), and inner (im) and outer muscular (om) layers. The OCT image correlates well with the histology in both the order of layers and the layer thickness. This result is in agreement with previous OCT imaging studies of the esophagus [38],

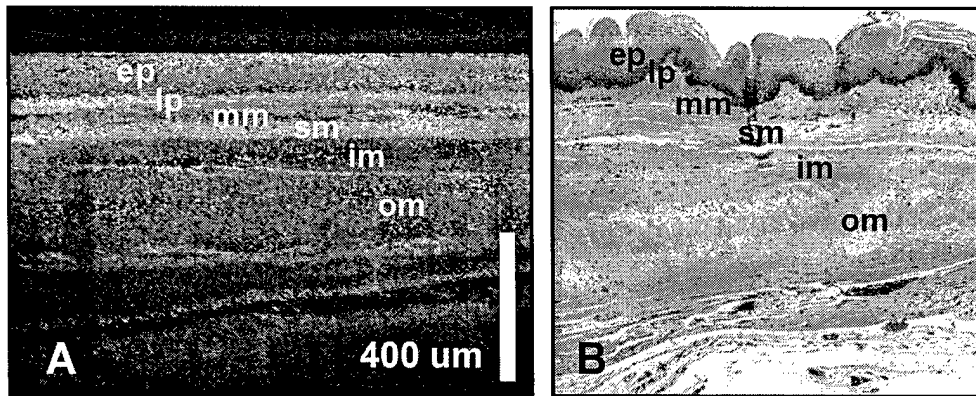


Figure 13. (a) *In vivo* endoscopic OCT image of rabbit esophagus with corresponding histology (b). Good correlation is seen between the OCT and histological cross sections for epithelium (ep), lamina propria (lp), muscularis mucosa (mm), submucosa (sm), and inner (im) and outer muscular (om) layers.

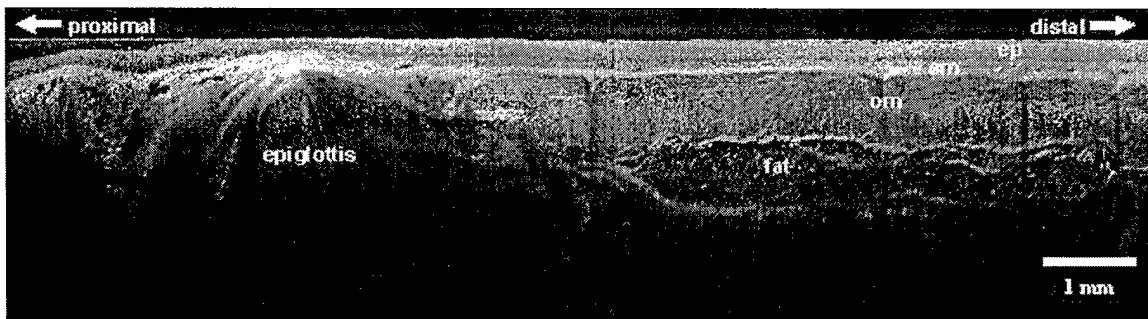


Figure 14. *In vivo* OCT image of sequential scans that span from the rabbit epiglottis to the inner esophagus. High resolution imaging is maintained over a large tissue field, allowing detailed discrimination of tissue structure.

while higher resolution provides more refined details of tissue morphology. Imaging of a larger tissue area was achieved by mechanically pulling back the imaging catheters and acquiring a series of images. Figure 14 shows a composite image of five OCT linear scans acquired sequentially as the catheter was withdrawn during imaging. Images were acquired over a 12 mm scanning range from the inner esophagus to the epiglottis. This image illustrates the capability of surveying tissue morphology over a large field at high resolution using endoscopic OCT system.

In Figure 15, an *in vivo* OCT image and a corresponding histology of the rabbit colon are shown. The OCT image shows a highly scattering and multistructured layer at the surface that correlates with the colonic mucosa. Individual crypts can be seen in the OCT image and they correlate well with the histology. The crypt features within the mucosa are visualized at greater detail in the 3x magnification images at the right side. Crypt boundaries within the lamina exhibit high scattering intensity in the OCT image, thereby increasing the contrast between individual crypts.

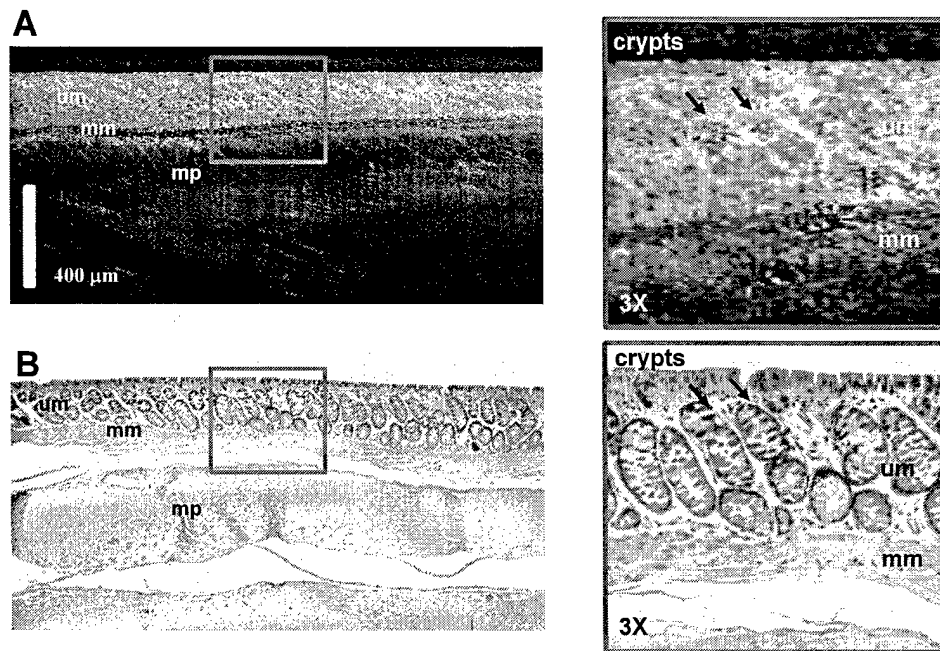


Figure 15. *In vivo* endoscopic OCT image of rabbit colon (a) with corresponding histology (b). Delineation of colon upper mucosa (um), muscular mucosa (mm), and muscularis propria (me) is possible. Enlarged images show the capability to visualize crypt structures in finer details.

The capability to resolve crypt features within the colon is important in the clinical diagnosis of conditions such as inflammatory bowel disease and colon cancer.

In summary, we have developed a high resolution endoscopic OCT imaging system and have obtained high resolution OCT images of the rabbit gastrointestinal tract with minimally invasive catheter devices. Using a compact, broadband Cr^{4+} :Forsterite laser, we demonstrated endoscopic OCT imaging *in vivo* at the highest resolution attained to date. A linear scanning protocol was used to generate high pixel density images at a real-time imaging rate of 4 frames per second. Histological cross sections were obtained from *in vivo* imaging sites and an excellent correspondence of architectural detail was seen between histopathology and OCT scans. Identification of clinically relevant tissue layers was possible at high resolution and is in agreement with histological findings.

These results demonstrate the feasibility of using high resolution endoscopic OCT for the identification of clinically significant architectural features in the gastrointestinal tract. We are currently applying the high resolution endoscopic OCT system in the clinical studies. Ongoing advances in the development of turnkey and portable broadband optical light sources promise greater access to high resolution OCT imaging capability for investigators.

Development of Optical Coherence Microscopy

Due to the significant clinical potential for a minimally invasive optical biopsy, several approaches have arisen [39]. These include confocal microscopy, multiphoton microscopy, and optical coherence tomography (OCT). These methods differ fundamentally in the means by which they section tissue, and these differences in sectioning method translate into differences in contrast, imaging depth, and available probe technology. None of these technologies has individually met all the needs of an optical biopsy tool. Confocal microscopy can provide high resolution cellular imaging, but it is limited in imaging depth and cannot be easily integrated into miniaturized imaging probes. Multiphoton microscopy also provides cellular resolution and can extend the imaging depth over confocal microscopy, but it is difficult to miniaturize. OCT provides the greatest imaging depth and, by contrast, lends itself to easy integration into miniature devices for widespread clinical application. Standard OCT techniques, however, cannot reliably reach the level of cellular imaging. In order to extend OCT imaging to the cellular level and to address the existing limitations of confocal and multiphoton microscopy, we are developing a method known as optical coherence microscopy (OCM). OCM is a novel extension of OCT and confocal microscopy that allows cellular imaging with superior imaging depth when compared to confocal microscopy alone and it facilitates the design of endoscopic and laparoscopic probes for cellular imaging. OCM promises to extend cellular imaging capability to the vast range of imaging applications previously available only to lower resolution imaging with optical coherence tomography.

OCM combines coherence-gated detection of OCT with confocal rejection of out-of-plane scattered light. These optical sectioning methods complement each other to provide enhanced imaging in highly scattering tissues. To achieve cellular-level imaging, OCM focuses to small spot sizes in tissue, as in confocal microscopy. OCT operates by fixing the focus at a specific depth in tissue and then scanning the coherence gate in the axial direction to generate a cross-sectional image. In order to maintain a sufficient depth of field over the extent of the image, OCT must operate with weaker focusing and lower transverse resolution. OCM is able to overcome this depth of field limitation because it scans an *en face* image plane similar to that of confocal microscopy and multiphoton microscopy. Figure 16 compares the imaging planes for OCM and OCT. In OCM, the position of the coherence gate is precisely matched to the optical focus at a specific depth in tissue and the beam is raster scanned in a two-dimensional *en face* pattern. Because the signal is recorded from a single depth in tissue, and not over a depth scan, a very tight focus can be maintained without the loss of signal that would occur in OCT. In focusing to a smaller spot size, the field of view in OCM must decrease, as in confocal microscopy. A cross-sectional OCT image spans 2-3 mm in each dimension, while a high resolution *en face* OCM image spans only 200-300 micrometers in each dimension, thus it represents only a small range of the OCT image.

OCM has the unique advantage of using two distinct optical sectioning techniques—confocal gating and coherence gating. Generally, the imaging point spread function in an OCM system is determined by the product of the confocal field point spread function $\sqrt{I_c}$ and the source autocorrelation function G , $I_d \propto \sqrt{I_c(z)} \times G(\Delta l)$, where z is the distance of the object from the microscope focus and Δl is the mismatch between the reference arm path length and the path length to the object. The confocal point spread function is entirely determined by the sample arm optics, and in particular, the numerical aperture of the final objective lens. The coherence gate, however, is determined by the light source bandwidth. The degree of confocal rejection of

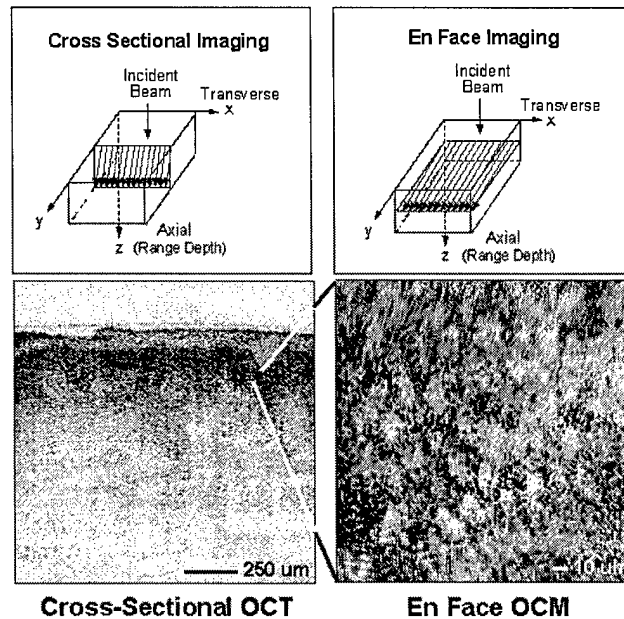


Figure 16. Scan planes for OCT and OCM. OCT scans a cross-sectional image plane and produces images of millimeter dimensions. OCM scans an *en face* image plane and achieves very high transverse resolution over small field of view that spans hundreds of micrometers.

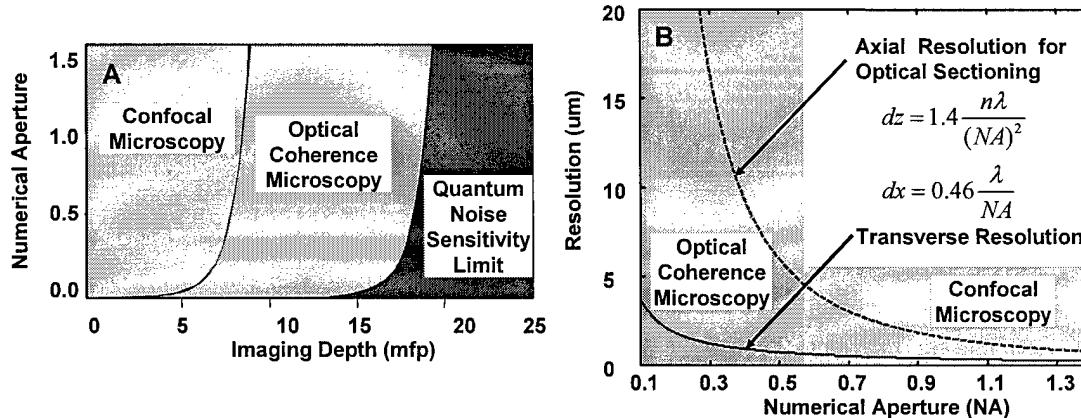


Figure 17. (a) Advantages of OCM when compared to confocal microscopy. OCM can provide increased imaging depth. (b) OCM can also image with high transverse resolution at much lower numerical aperture than confocal microscopy, because it does not depend on high axial resolution for optical sectioning.

unfocused scattered light can be varied by changing the numerical aperture of the objective lens, while the amount of coherence gated sectioning can be varied by changing the bandwidth of the light source. The multiplicative effect of the two sectioning methods strengthens the overall optical sectioning power, thus allowing increased rejection of unwanted, out-of-focus scattered light. Studies from our group, as well as others have demonstrated that combined confocal and

coherence gating can provide improved imaging depth when compared to confocal gating alone [40-42]. Figure 17(a) illustrates the imaging depth advantage of OCM. The addition of high-sensitivity coherence-gated detection to confocal detection extends the imaging depth in scattering media to the shot noise quantum limit, thus providing a factor of 2-3 increase over standard confocal microscopy.

The use of multiple optical sectioning techniques also allows considerable flexibility in system design for achieving high-resolution cellular images. In one limit, high numerical aperture (NA) optics can be used to produce very thin confocal tissue sections, while relatively weak coherence gating can be added to improve rejection of unwanted light. In the other limit, broad-bandwidth light sources as used in ultrahigh resolution OCT can provide thin optical sectioning via coherence gating, and the confocal sectioning can be relaxed to facilitate development of miniaturized imaging devices. Figure 17(b) compares the confocal axial and transverse imaging resolution as a function of the numerical aperture of the probe optics in order to demonstrate this operating limit for OCM. The axial section thickness degrades much more quickly than the transverse resolution, and there exists a region where the transverse resolution is sufficient for cellular imaging but the axial resolution is not. Addition of a short coherence gate to provide tissue sectioning can, therefore, make cellular imaging possible with a much lower NA than what is sufficient for confocal microscopy alone. This operating regime for OCM imaging has very important clinical implications, since it promises to allow cellular imaging with small-diameter probes that are compatible with standard endoscopic and laparoscopic procedures.

Recently, we extended previous theoretical work on OCM in order to develop an OCM system suitable for *in vivo* clinical imaging applications [43]. Such a system needs to be capable of high-speed imaging to minimize the amount of motion artifacts in images. In addition, the system should support broad optical bandwidths, as in ultrahigh resolution OCT, to take full advantage of the optical sectioning ability of OCT. Previous attempts at high-speed, high-resolution OCM imaging were limited by the lack of high-speed, broadband phase modulators. Based on previous OCT phase delay scanners [44, 45] and femtosecond pulse shaping devices [43, 46, 47], we designed a novel reflective grating phase modulator capable of performing continuous phase modulation of broadband laser light. Figures 18(a) and 18(b) illustrate the phase modulator design in its top and side views. A collimated beam is spectrally dispersed by a grating onto a curved mirror. The curved mirror captures and focuses the diffracted beam onto the galvanometer mirror, which imparts a wavelength-dependent phase shift in the Fourier plane. The modulator is set for double-pass configuration to increase the delay characteristics and to improve backcoupling of the scanned beam. Use of a relatively low dispersion grating and a short focal-length mirror results in zero group delay at a realizable beam offset from the center axis of the scanning mirror. Furthermore, large phase delays of > 1700 radians per degree of mirror rotation can be achieved. Most importantly, the reflective nature of the design allows the modulator to support a large optical bandwidth, thus enabling high resolution OCM imaging.

The imaging system diagram, including the grating phase modulator, is shown in Figure 19. Light from a broadband femtosecond laser source is coupled into a fiber optic interferometer, which splits the light equally between the broadband phase modulator and a scanning confocal microscope. Light returning from the phase modulator and from the tissue is recombined at a pair of balanced detectors to produce the image interference signal, which is then demodulated

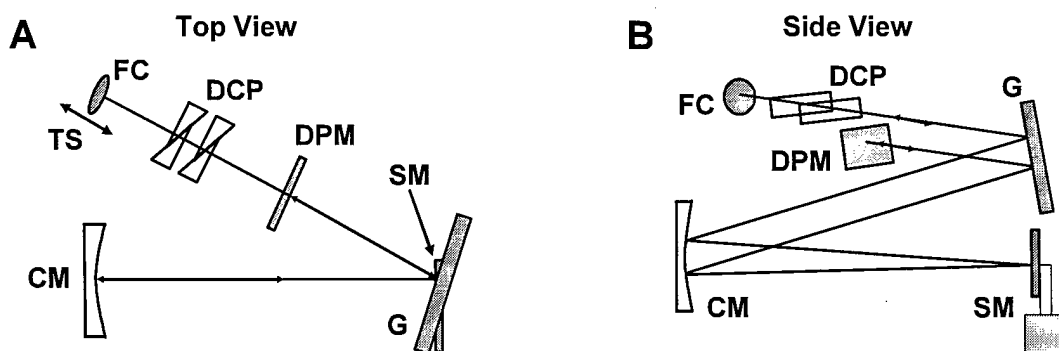


Figure 18. Schematic of reflective grating phase modulator in top (a) and side (b) views. TS, translation stage; FC, fiber collimator; DCP, dispersion compensating prisms; G, grating; CM, curved mirror; SM, scanning mirror; DPM, double-pass mirror. The modulator supports broad optical bandwidths that enable high resolution OCM imaging.

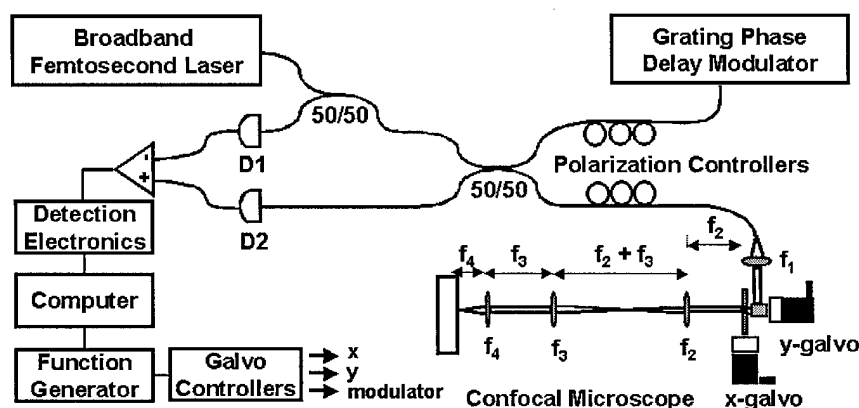


Figure 19. Schematic of broadband, high resolution OCM system.

electronically and displayed on a computer screen. The fiber optic geometry makes the system ready for integration with a variety of catheter-based devices for clinical applications. This OCM system is the first system demonstrated that is capable of performing high-speed, high-resolution OCM imaging with broadband femtosecond laser sources.

Using this system, we verified for the first time the ability to use combination coherence gating and confocal gating to image cellular features when confocal microscopy alone would be inadequate. In particular, the results show that strong optical sectioning achieved with a short coherence gate can mitigate the need for high numerical aperture confocal optics. Figure 20 demonstrates this concept. A short coherence gate of $\sim 3 \mu\text{m}$ is combined with a confocal gate of $\sim 30 \mu\text{m}$. While this confocal section thickness is nearly six times that of standard histology, a high transverse resolution can still be maintained, as shown by imaging the smallest features of

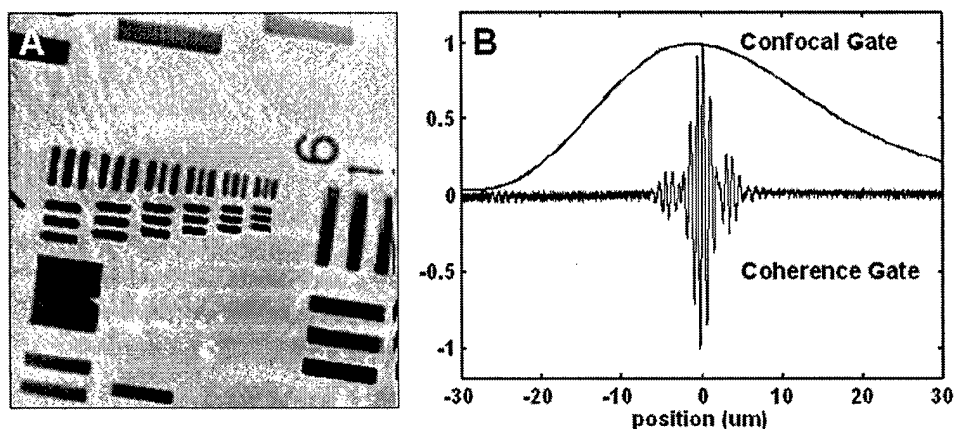


Figure 20. OCM system characterization. A short coherence gate is used to compensate a longer confocal gate, which will moderate probe design constraints on endoscopic imaging. High transverse resolution is maintained, despite weaker confocal sectioning.

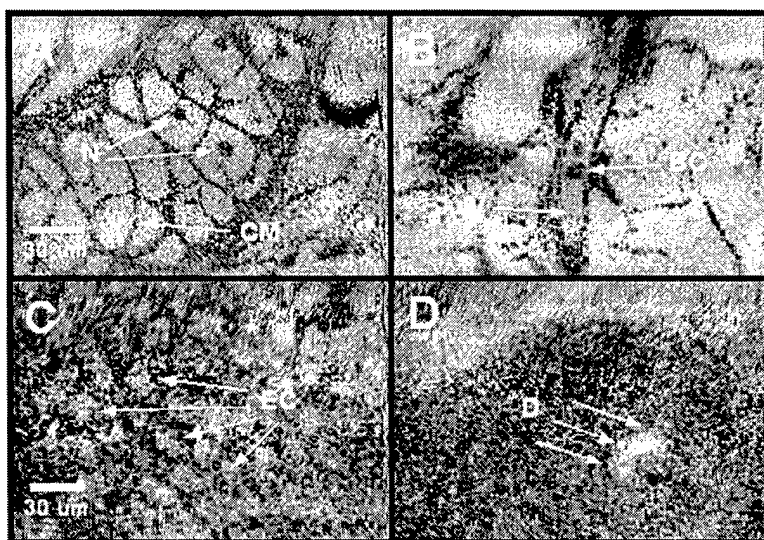


Figure 21. *In vivo* OCM cellular imaging in *Xenopus laevis* tadpole (A,B) and human skin (C,D). Nuclei (N), cell membranes (CM), and blood cells (BC) inside a vessel (V) are visible in the tadpole images, and epidermal cells (EC) and a vessel or duct structure (d) in the dermis can be seen in the skin images. The images were acquired at 800 nm wavelength at 4 frames per second.

the USAF resolution target, which measures $4.4\ \mu\text{m}$. The combined gating effects are sufficient for high-resolution *in vivo* imaging of cellular features in various tissues, as demonstrated in *Xenopus laevis* tadpole and in human skin in Figure 21. In *Xenopus* tadpole, nuclei (N), cell membranes (CM), and blood cells (BC) inside a vessel (V) are visible, while in human skin, epidermal cells (EC) and a vessel or duct structure (d) in the dermis can be visualized.

Demonstration of this operating limit for OCM marks an important advance because it opens the door for the development of multiple miniaturized OCM imaging probes. Eliminating the need for high NA confocal sectioning will significantly mitigate the design constraints on catheter and rigid endoscope design. Future work will include the demonstration of OCM imaging of multiple tissue types and important pathologies, as well as the development of miniaturized OCM imaging devices for endoscopic and laparoscopic applications.

Spectroscopic Optical Coherence Tomography

Standard optical coherence tomography generates a two-dimensional map of backscattered intensity from tissue. Broadband laser sources are used to precisely localize light from small volumes via coherence-gated detection, thereby enabling high-resolution imaging of tissue microstructure. Beyond providing high spatial resolution, the use of broadband sources also provides access to wavelength dependent absorption and scattering in tissue. Spectral information obtained from the OCT interference signal can be used to quantitatively probe the functional state of tissues through correlation of spectral changes with the known absorption or scattering characteristics of tissue constituents. Furthermore, the combination of spectroscopic information with structural images provides an alternate mode of contrast for OCT images. Because intrinsic image intensity contrast in tissue is low, such contrast enhancement is an important area of research to improve the diagnostic capability of OCT.

Relatively few studies on spectroscopic OCT have been performed because suitable broadband light sources have not been available. Spectroscopic OCT was demonstrated initially using a bandwidth of ~ 50 nm at a center wavelength of $1.3\ \mu\text{m}$ [48]. Studies in the spectral region of the water absorption band at $1.45\ \mu\text{m}$ were performed using two different light sources in dual wavelength OCT systems. One wavelength was used for absorption measurements and the second light source for referencing [28, 49]. Our group has had a sustained interest in developing spectroscopic OCT for clinical applications.

The technique for spectroscopic OCT imaging is based on short time Fourier transform (STFT) analysis. By applying sequential shifts of a local one-dimensional windowing function to each A-scan, and calculating the Fourier transform of the windowed data, an approximate local spectrum can be calculated for every pixel in the image. This requires the complete interference fringe to be acquired and processed using DSP technology. If the sample being imaged were a perfect mirror, the calculated spectra would be identical to the laser spectrum. Spectroscopic analysis produces a four-dimensional data set consisting of x and y spatial coordinates, an RF frequency equivalent to an optical wavelength, and spectral amplitude. To create an interpretable image, it is necessary to condense this information into three dimensions. This forms the critical step in spectroscopic OCT analysis, since the metric chosen to describe the spectrum at each pixel strongly affects the contrast enhancement of the system as well as the types of spectroscopic properties that will be visible. Metrics based on spectral modulation, which constitute an indirect measurement of scattering particle size, were developed and applied to developmental biology specimens. Traditional center wavelength analyses were also carried out on scattering tissue samples, such as the hamster cheek pouch, thus demonstrating the ability to detect deeply buried blood vessels *in vivo*.

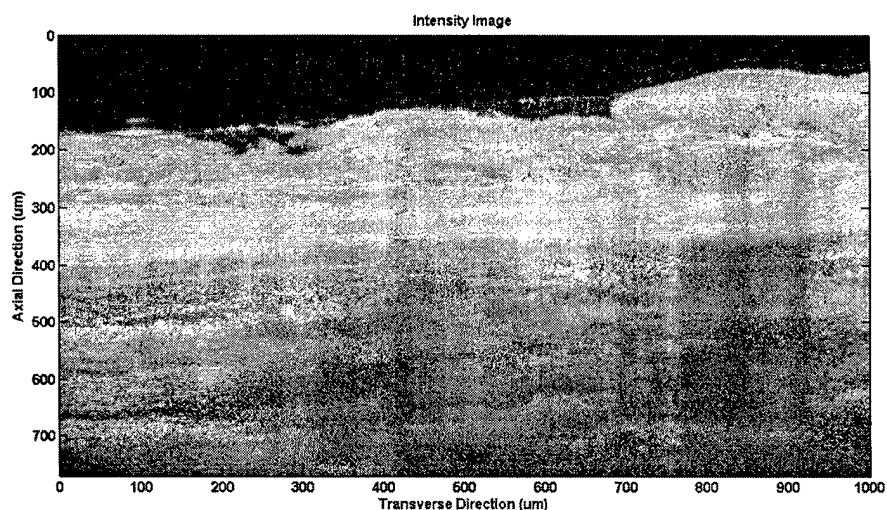


Figure 22. Standard *in vivo* intensity-based OCT image of Syrian golden hamster cheek pouch. Structural features are clearly visualized and blood vessels (V) are visible in upper right portion of image.

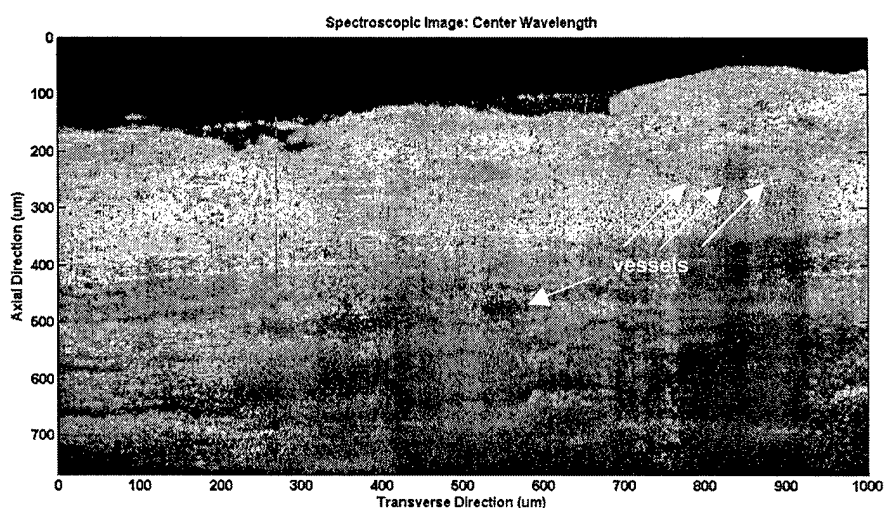


Figure 23. Spectroscopic OCT image of Syrian golden hamster cheek pouch, acquired *in vivo*. Red and green colors indicate red-shifting and blue-shifting of the detected spectra, respectively. Blood vessels are clearly visible, including a deeply buried vessel not visible with intensity-based OCT imaging.

Figure 22 shows a standard intensity-based OCT image of a Syrian golden hamster cheek pouch, acquired *in vivo*. Figure 23 shows the same image after spectroscopic analysis, where the color indicates variations in the center wavelength of the detected spectra. Red colors indicate red-shifting of the spectra, while green colors indicate blue-shifting of the spectra. Blood vessels are clearly visible in Figure 23 as areas of significant red- and blue-shifting, including one deeply buried vessel not visible under standard OCT analysis.

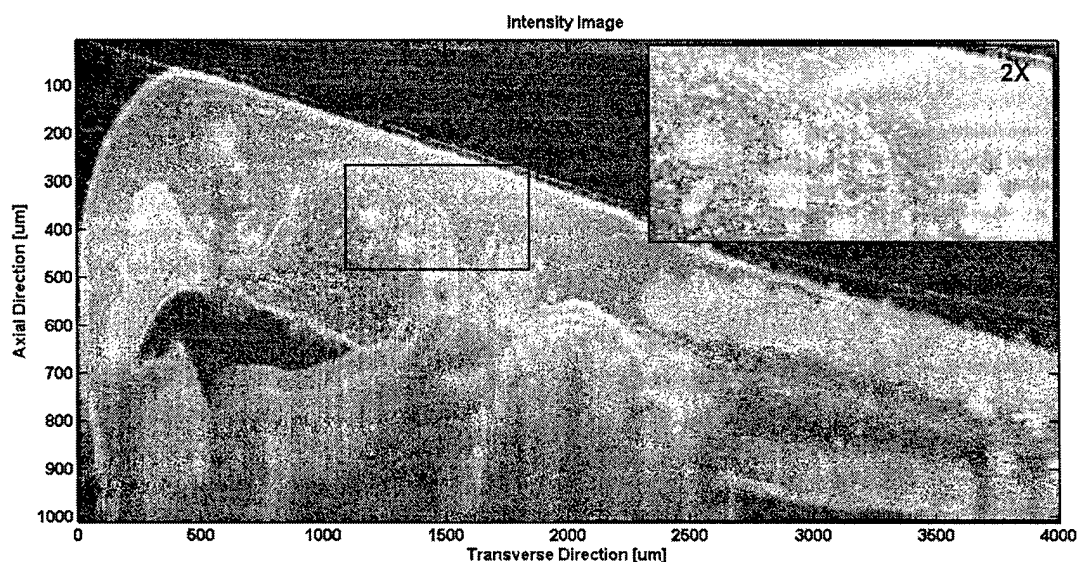


Figure 24. Standard *in vivo* intensity-based OCT image of a developing *Xenopus Laevis* (African frog) tadpole.

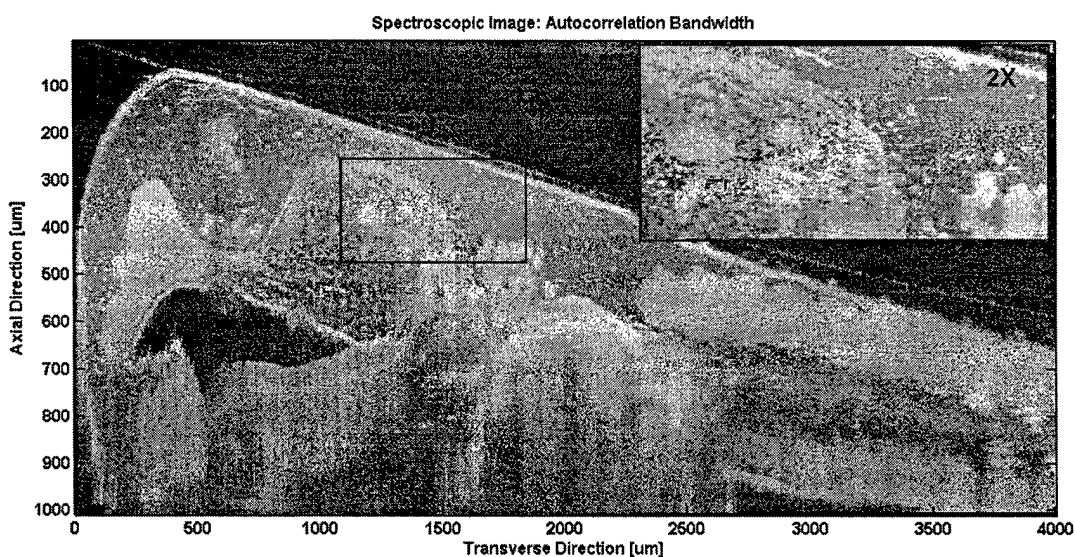


Figure 25. *In vivo* spectroscopic OCT image of a developing *Xenopus Laevis* (African frog) tadpole, using spectral modulation to generate the color overlay. Red regions indicate low spectral modulation, while blue areas high spectral modulation. Spectroscopic contrast is obtained between the various tissue types of the organism.

Spectroscopic analysis based on a calculation of the center wavelength of the detected spectra is useful, but other analysis methods can be used to provide alternative contrast modalities. For example, there is a correlation between the size of biological scattering particles and the spectral

modulation observed by interferometry [50-57]. Central to this method is the idea that cellular organelles of epithelial tissue can be considered as spherical scatterers whose interactions with light are governed by Mie theory [58, 59]. By quantifying the spectral modulation at each pixel in a spectroscopic OCT image, it is possible to differentiate tissue types based on the size of the scattering particles contained in the tissue. Figure 24 shows a standard intensity-based OCT image of a developing *Xenopus Laevis* (African frog) tadpole. Figure 25 shows the same image after spectroscopic processing, using an analysis of spectral modulation to generate the color overlay. Here, red colors indicate areas of low modulation, while blue colors indicate areas of high modulation. The various tissue types of the tadpole are differentiated based on the scattering particle sizes contained in the tissues. This method may eventually enable the detection of early-stage epithelial cancers, which are characterized by an abnormal proliferation of epithelial basal membrane cells having organelle sizes that differ from surrounding cells.

Ultrahigh Speed OCT Imaging using Fourier Domain Techniques

Ultrahigh resolution optical coherence tomography (OCT) has improved the differentiation of architectural morphology in the retina and can visualize subtle changes associated with early disease [6, 60]. One limitation of standard OCT using time domain detection is that high resolution imaging requires a decrease in imaging speed. Because light exposure levels in the eye are limited, the imaging speed possible with a time domain detection system is limited by the minimum sensitivity required for good image quality. New techniques known as Spectral/Fourier domain detection have recently been developed which enable dramatic improvements in imaging speed and sensitivity [61-63]. With the higher speeds enabled by OCT with spectral/Fourier domain detection, it is possible to form three-dimensional maps of the macula and optic disk *in vivo*. This enables cross-registration of three-dimensional data sets with fundus photographs for a more accurate diagnosis of disease and evaluation of treatment outcomes. Video-rate movies of dynamic processes in the eye are also possible. High-quality images can be generated by oversampling in the transverse direction and by averaging data, which allows for the enhanced visualization of intraretinal layers and better segmentation. Furthermore, spectral/Fourier domain OCT provides direct access to the spectral fringe pattern, thus enabling a wide range of novel applications in Doppler flow imaging [64], absorption measurement [65], dispersion compensation [66], and complex spectral analysis [67].

In OCT with spectral/Fourier domain detection, a spectrometer with a multichannel analyzer is used to acquire and process the spectral components of the optical signal. Backreflected or backscattered light from all axial depths in the sample is acquired simultaneously as an interferometric spectrum and is processed in software in order to obtain the axial or depth scan. This method is different than time domain detection, where a reference arm with a variable delay is scanned and data from different axial depths is sequentially acquired. A schematic of the spectral/Fourier domain ultrahigh resolution ophthalmic system is shown in Figure 26. Note that the reference arm is stationary, a spectrometer and CCD camera are used in place of time domain electronics, and the software processing is computationally more intensive. Because of its detection method, spectral/Fourier domain OCT has an inherent sensitivity and/or speed advantage over time domain OCT. In time domain OCT, the signal noise increases with increasing detection bandwidth. Since ultrahigh resolution requires broadband sources and high optical bandwidths, the imaging speed must be reduced so that the electronic detection

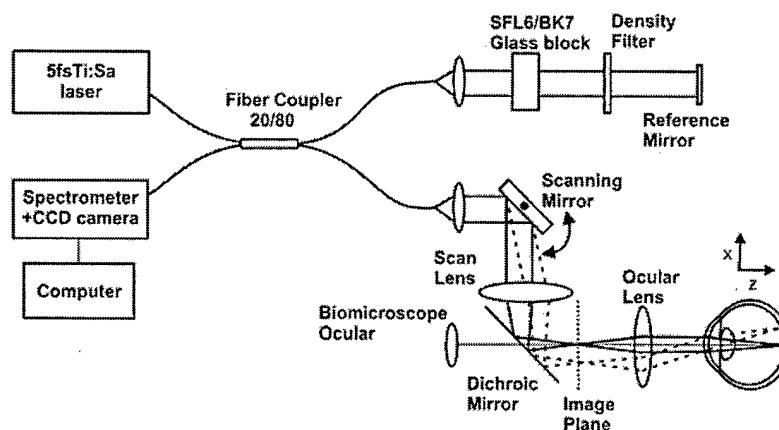


Figure 26. Schematic of ultrahigh resolution system OCT with spectral/Fourier domain detection. Retinal imaging was performed using a slitlamp biomicroscope. The spectrometer consisted of a collimating lens, a transmission grating, and a lens that imaged the spectrum onto a 2048-element-line-scan CCD.

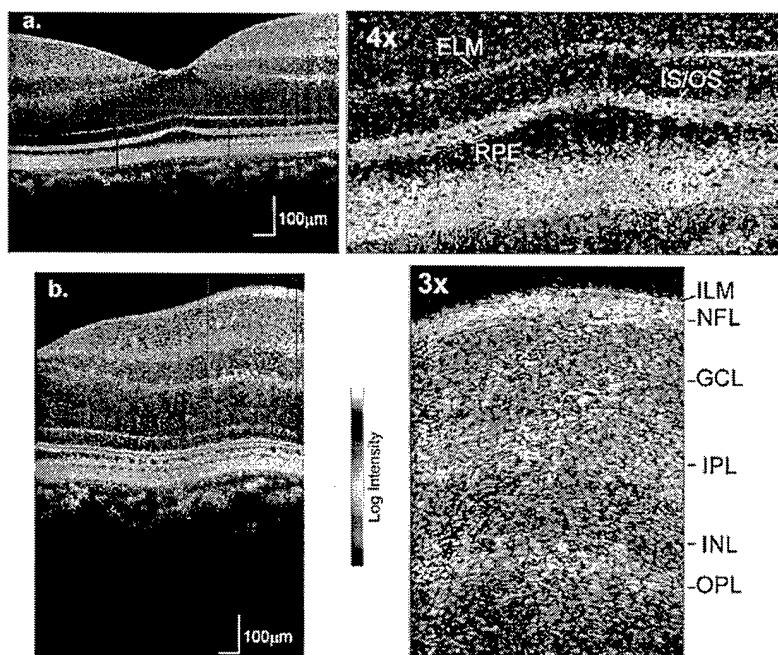


Figure 27. Spectral/Fourier domain OCT images of the human retina *in vivo*. Images with 3000 axial scans area acquired in 150 ms. (a) The high transverse pixel density and axial resolution allows better visualization of retinal layers, including the external limiting membrane (ELM), photoreceptor inner and outer segment junction (IS/OS), and retinal pigment epithelium (RPE). (b) The inner limiting membrane (ILM) can also be discriminated from the nerve fiber layer (NFL) in the 3x image.

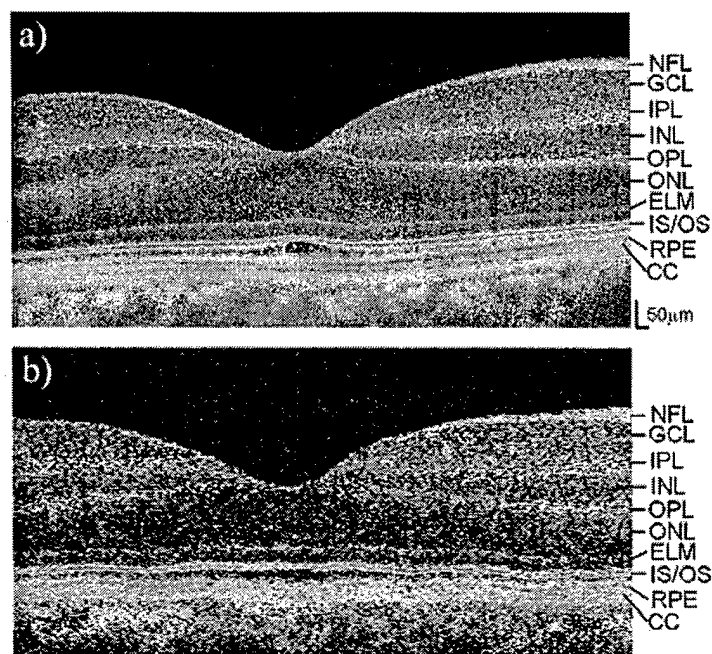


Figure 28. Comparison of ultrahigh resolution spectral/Fourier domain OCT (a) and standard ultrahigh resolution OCT (b).

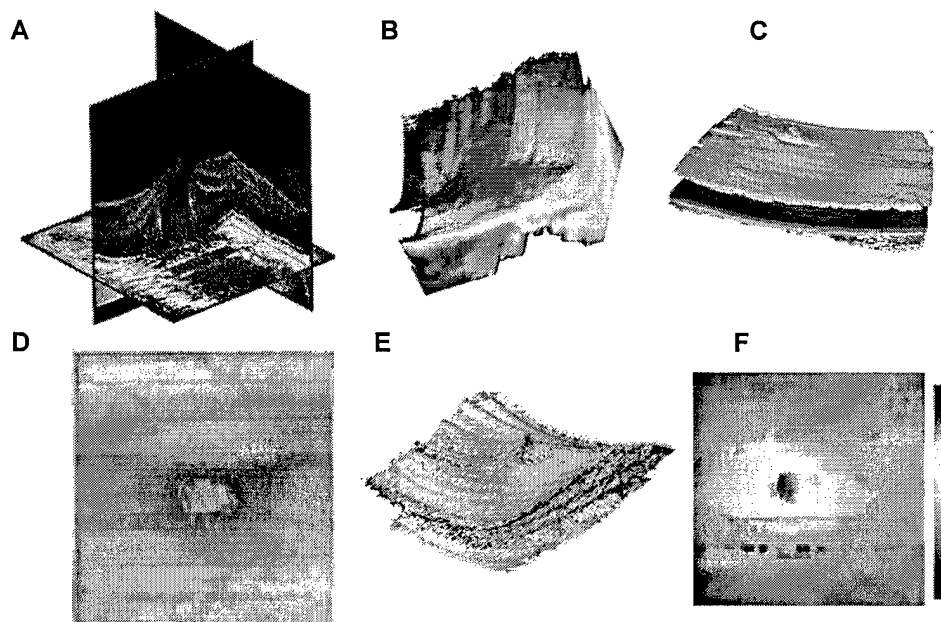


Figure 29. Three-dimensional reconstructions of full thickness macular hole: (a) ortho-slices; (b) virtual rendering; (c) retinal segmentation; (d) en-face view; (e) surface topographic view; (f) full thickness mapping.

bandwidth decreases and the image quality is maintained. Alternatively, the imaging speed may be increased if a reduction in sensitivity can be tolerated. With spectral/Fourier domain OCT, no such penalty in sensitivity is incurred by increasing the source bandwidth.

Spectral/Fourier domain OCT was recently applied to retinal imaging [68] and has been shown to achieve better imaging speed and sensitivity than time domain OCT [62, 69]. Recently, video-rate retinal *in vivo* imaging was demonstrated [70]. Our group demonstrated high-speed, ultrahigh resolution retinal imaging by using spectral/Fourier domain OCT [66]. We achieved an axial resolution of 2.1 μm using a 5 fs Ti:Sapphire laser light source [71] and a broadband spectrometer design. Acquisition of 16,000 axial scans per second with 1024 pixels per axial scan was achieved using a 12-bit, 2048-pixel-line-scan camera. The system sensitivity was 98 dB, thus yielding excellent image quality as shown in Figure 27. Spectral/Fourier domain OCT enables an increase of 100x in imaging speed over ultrahigh resolution time domain OCT imaging. A comparison of spectral/Fourier and time domain ultrahigh resolution images is shown in Figure 28. The spectral/Fourier OCT image of 3000 axial scans was acquired in 150 mw, while the ultrahigh resolution time domain image of 300 axial scans was acquired in 2 seconds. We have also developed an efficient software procedure for automatic dispersion compensation, an important factor in achieving ultrahigh resolution [66]. We have built a clinical spectral domain OCT system using a low-threshold, compact Ti:Sapphire laser[15], and have demonstrated three-dimensional imaging of retinal pathologies in collaboration with the New England Eye Center at the Tufts-New England Medical Center, as shown in Figure 29. We will continue to research the applications of spectral domain OCT through clinical studies, as well as conduct basic research on system design and imaging techniques.

Optical Biopsy and Novel Devices for Clinical Applications

Optical Coherence Tomography (OCT) permits the visualization of tissue microstructures *in vivo* and *in situ*, with resolutions of 1-15 μm . Like conventional biopsy and histology, OCT can provide three-dimensional cross-sectional images that may allow differentiation of normal from diseased tissues. However, unlike histology, OCT can be performed in real-time and without the need of tissue excision, thus increasing its possible application areas in where the excision biopsy is impossible or undesirable, and potentially allowing the use of OCT in guidance of biopsy or surgery.

We are investigating the use of OCT in imaging a variety of clinically relevant tissue types and pathologies, for application in clinical diagnosis and treatment, and for basic biomedical research. Integration of high resolution OCT into portable systems described previously offers promise to expand the use of OCT in *in vivo* and *ex vivo* imaging in the clinic. These technologies include advanced imaging techniques themselves as well as sophisticated diagnostic probes that enable the imaging of internal body organs that would otherwise be inaccessible to various imaging modalities. Such devices are critical for the implementation and realization of OCT as a diagnostic imaging modality, since OCT image penetration is limited to the first several millimeters of a tissue surface. In this section, the design, development, and use of minimally invasive catheter-based probes used in OCT systems will be described.

Micromotor Catheter Probe for Endoscopic Imaging

Minimally invasive endoscope-catheter imaging probes that can focus and scan a beam inside the body have been an important technology for enabling endoscopic OCT imaging studies. The most common probe design uses a mechanical cable, an optical fiber, and a lens assembly housed in a transparent plastic sheath. The cable within the sheath is either rotated or translated in a push-pull motion to produce a rotary or linear scanning motion of the optics in order to generate a transverse or longitudinal OCT image. However, because the distal optics are actuated from the proximal end of the long probe, this design can result in a non-uniform scanning motion that introduces artifacts in the OCT image. Imaging speeds and duty cycles are limited. In addition, for rotary scan designs, a proximally located rotary optical coupling is required. Forward imaging designs avoid these problems, but scan ranges can be limited. Recent developments in novel MEMS scanning technologies promise distal beam scanning, which would improve the speed and reduce image distortion in endoscopic imaging [72, 73]. Despite these advances, previous endoscope-catheter probe designs could not provide focus adjustment during OCT imaging. For this reason, relatively large spot sizes were necessary in order to preserve a sufficient depth of field to enable OCT imaging in intraluminal structures. This limits the transverse image resolution.

We recently developed a new, high resolution, micromotor endoscope-catheter with adjustable focus capability. The mechanical scanning and micro-optic components are located at the distal end of the probe, thereby eliminating the need for proximally actuated rotating or translating elements. Distal actuation provides better uniformity of beam scanning with reduced image distortion artifacts and an improved range of image speeds. Standard OCT imaging probes usually require long depth of fields and, therefore, the minimum transverse focused beam sizes are limited. With the ability to independently adjust the optical beam focal position and use higher numerical aperture optics, transverse image resolution can be improved. In addition, an adjustable focus device can enable C-mode OCT imaging (acquiring images with several focal planes and fusing them together) to overcome depth of field limitations [7]. The micromotor imaging probe also has a larger field of view than conventional OCT endoscope-catheter devices, thereby allowing larger diameter lumens to be more readily visualized.

Figure 30 shows a schematic and photograph of the micromotor endoscope-catheter probe assembly. The probe consists of a distally actuated micromotor and an optical assembly for the beam focusing. The micromotor is a commercially available subsystem (manufactured by Micro Precision Systems AG), which consists of a three-phase brushless DC motor. It has a planetary gearhead design and is configured with a 125:1 gear reduction ratio. A vertical Hall sensor built into the motor is used to accurately control and stabilize the rotation speed with a 5V operating voltage. The optical assembly consists of a GRIN lens collimator and an achromatic focusing lens that move independently of the probe sheath (in a longitudinal direction) in order to adjust the focus position within the tissue.

The transverse resolution of the focused optical beam was measured at $\sim 8 \mu\text{m}$ ($2\omega_0$ spot diameter) by using a knife-edge beam profile technique. The corresponding depth of field or confocal parameter is $\sim 80 \mu\text{m}$ at a 1250 nm center wavelength. An aluminum-coated rod mirror is mounted onto the motor shaft to direct the focused light onto the tissue and to enable a rotational OCT scan. The motor speed can be adjusted, thus enabling rotation speeds from 1 Hz

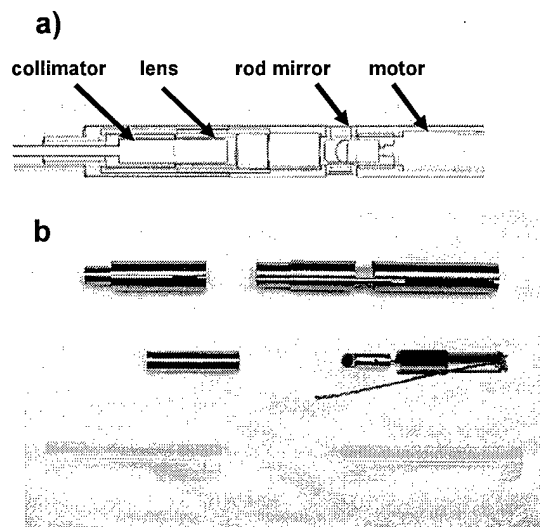


Figure 30. Schematic and photograph of the micromotor catheter assembly and components. (a) Wireframe cutaway with fiber collimator, focusing lens, rod mirror, and micromotor enclosed in housing. (b) Stainless steel housing and catheter components photographed before assembly. The micromotor is shown with the rod lens attached.

to 100 Hz. The motor and distal optics fit within a 4.8 mm OD stainless-steel housing, which is enclosed within a 5 mm OD transparent plastic sheath. Control wires to actuate the motor are fed through the tubing to the proximal end of the probe. The fiber collimator and focusing lens are attached to a mechanical speedometer cable, which enables the distal focus to be adjusted by translating the fiber and lens assembly with respect to the fixed scanning motor at the distal end.

The OCT interferometer, which consists of a broadband optical circulator and 90/10 fiber optic beam splitter, transmits 90% of the light into the sample arm and 10% into the reference arm. Dual-channel detection acquired by using polarization diversity is used before digital signal demodulation. A rapid scanning delay line is used in the system reference arm with 2000 axial scans per second. This corresponds to 1000 axial scans per OCT image at a 2 Hz image frame rate. For a probe diameter of 5 mm, this gives a transverse pixel spacing of 15 $\mu\text{m}/\text{pixel}$ along the probe circumference. A broadband femtosecond Cr:Forsterite laser and nonlinear optical fiber are used as the light source. The measured axial image resolution in air is 5 μm , which corresponds to a resolution of $\sim 3.7 \mu\text{m}$ in tissue. The imaging scan depth is 4 mm and the axial pixel spacing is 2 $\mu\text{m}/\text{pixel}$. The sensitivity is 92 dB at an incident power of 12 mW.

In order to demonstrate the micromotor endoscope-catheter probe, *in vivo* OCT imaging was performed on an anesthetized New Zealand white rabbit. Animal handling was performed in accordance with protocols approved by the MIT Committee on Animal Care. Imaging was performed on the colon, because the columnar epithelial structure of colonic mucosa provided well-defined tissue morphology for validation of the adjustable focus probe operation. To minimize animal discomfort and to reduce the risk of damaging the colonic mucosa, a sterile

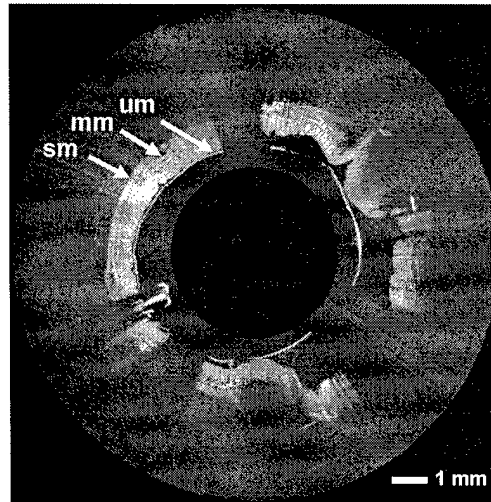


Figure 31. OCT image of rabbit colon *in vivo* with $<4 \mu\text{m}$ axial resolution. Visualization of colonic upper mucosa (um), muscularis mucosae (mm), and submucosa (sm) layers is possible. Shadowed regions at 11, 4, and 7 o'clock positions are support struts that occlude part of the scan field.

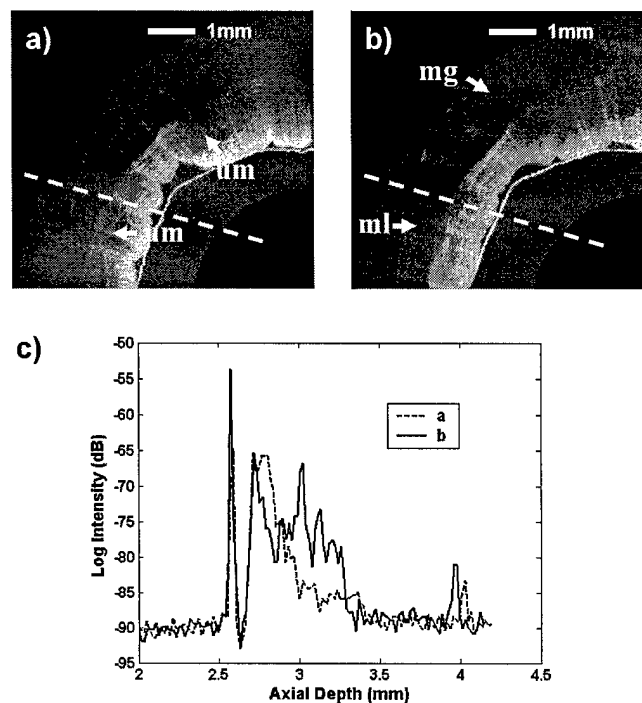


Figure 32. OCT images at two different focus settings. (a) Focus near the tissue surface provides a higher contrast within the colonic upper mucosa (um). (b) Setting the focus $500 \mu\text{m}$ deeper enhances deeper mucosal layers (ml) and glandular structure (mg). (c) Plots of axial scans along the dashed lines for the two focus depth settings (a and b).

bacteriostatic lubricant was used during catheter insertion. Multiple locations within the colon were imaged. At each imaging position, OCT scans were taken at several focus depths to demonstrate the adjustable focusing capability of the probe. The beam focal depth was changed by translating the collimator and focusing lens assembly with respect to the fixed motor assembly.

This micromotor imaging probe design has several attractive features. Adjustable focus enables smaller focused spot sizes and a shorter depth of field than what was previously feasible. The resulting improvement in image resolution could improve the performance of ultrahigh resolution OCT imaging by enabling a better visualization of tissue pathology. With additional engineering, it should be possible to perform dynamic focusing, where the focal position is adjusted as a function of rotary beam position. This would enable focus tracking in cases where the endoscope-catheter probe was not centered in the lumen. The use of a micromotor for distal actuation reduces the motion non-uniformity that could occur with previous proximally actuated endoscope catheter probes. A wider range of imaging speeds can be achieved with improved duty cycle. Finally, although this prototype imaging probe was 5 mm in diameter, a reduction in probe size is possible with smaller micromotors.

In conclusion, a new micromotor endoscope-catheter imaging probe for OCT has been developed. This device enables focus adjustment and ultrahigh resolution endoscopic imaging. *In vivo* endoscopic imaging was demonstrated in an animal model and ultrahigh resolution imaging with $<4\text{ }\mu\text{m}$ axial resolution was demonstrated. This new design promises to improve imaging performance in future endoscopic OCT imaging studies.

MEMS Scanner for Endoscopic OCT

Optical coherence tomography (OCT) is an emerging technology for high-resolution endoscopic imaging of biological tissues *in situ* and in real time [38]. Endoscopic OCT can distinguish architectural layers *in vivo* and can differentiate normal from tumor lesions within the human gastrointestinal tract. A need for compact, robust scanning devices for endoscopic applications has fueled the development of MEMS scanning mirrors for confocal imaging [74, 75] and for optical coherence tomography [72, 73]. Demonstrations of MEMS scanning OCT endoscopes, however, have been limited to single-axis scanning. The ability to use two-dimensional (2D) scanners would be an important advance that would permit three-dimensional (3D) imaging *in situ*.

The most important requirement for a MEMS imaging scanner is high resolution. The resolution of an angle scanning device is determined by the angular scan range divided by the angular divergence of the beam that it can scan, commonly known as the number of resolvable spots. To achieve 1000 or more resolvable spots for high resolution imaging, a large optical aperture and a large scan range must be achieved. High scan speed, in the hundred Hz to multiple kHz, is also important for real-time imaging and the footprint of the scanner must be small to allow for easy integration into miniaturized devices. Finally, low power actuation is also necessary to avoid risks to the patient.

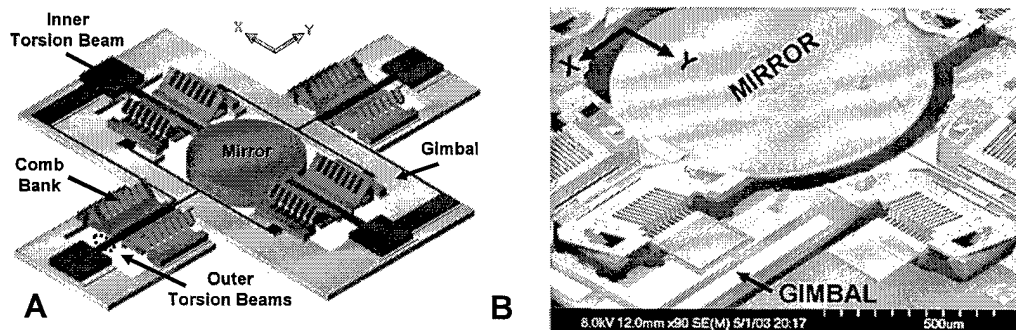


Figure 33. Schematic (a) and SEM (b) of the 2D MEMS scanning mirror. The mirror was realized by a combination of surface-micromachining and deep-reactive-ion-etching (DRIE). It offers a large mirror in a small form factor that enables large optical aperture and miniaturized device integration.

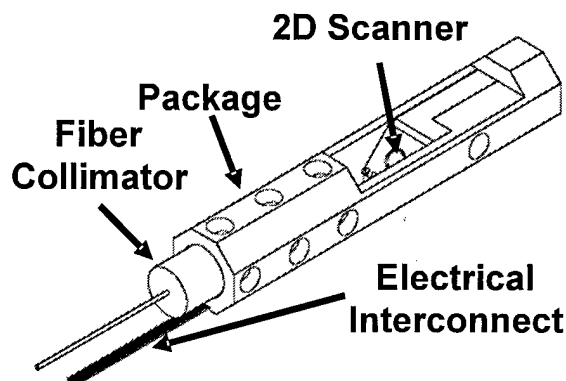


Figure 34. Schematic of packaged MEMS endoscope. The entire device measures less than 6 mm in diameter and can be further reduced in size.

We are collaborating with Professor Ming Wu, one of the leading optical MEMS groups at the University of California at Los Angeles (UCLA). The UCLA group was first to demonstrate a two-dimensional surface micromachined scanner [76]. As part of a program also sponsored by the National Science Foundation, the UCLA and MIT groups have designed and fabricated novel single- and dual-axis high resolution MEMS scanning mirrors, based on a novel electrostatic angular vertical comb (AVC) drive approach [77]. Figures 33(a) and 33(b) show the schematic and SEM of a typical mirror. Comb drive actuators can significantly reduce the scan drive voltage and extend the scan range, as compared to previous parallel-plate scanner designs. The scanner is realized by combining a foundry surface-micromachining process (Multi-User MEMS Processes, MUMPs) with a three-mask deep-reactive-ion-etching (DRIE) post-process. Surface-micromachining provides versatile mechanical design and electrical interconnect, while bulk micromachining offers flat micromirrors and high-force actuators. The actuator uses torsion beams and a gimbal-mounting configuration in order to scan on two axes. Furthermore, our mirror designs implement a large mirror surface area in a small overall form factor that enables large optical aperture and miniaturized device integration.

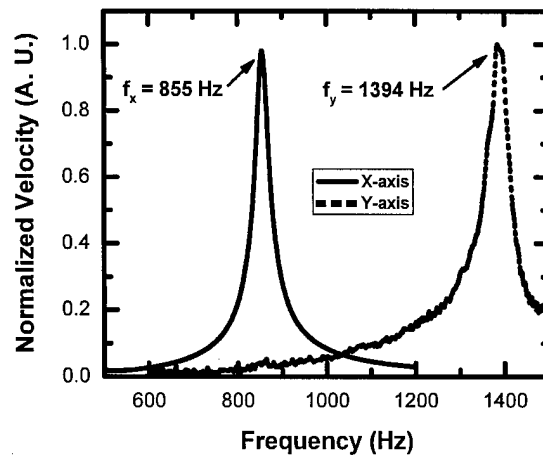


Figure 35. Frequency response of the two-dimensional MEMS scanner. High-speed resonant scanning should enable endoscopic microscopy applications.

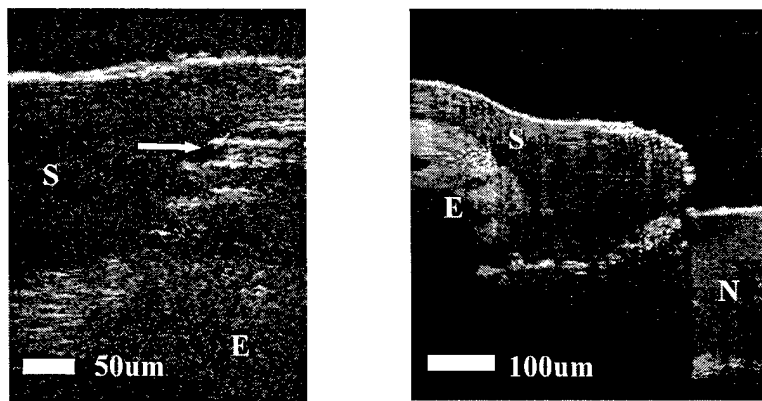


Figure 36. OCT images obtained with the 2D MEMS scanner. (a) *In vivo* image of human skin showing the delineation of stratum corneum (S), epidermis (E), and a spiraling sweat duct (horizontal arrow). (b) Image of human nail fold obtained at 20 frames per second with 4 frame averaging, with stratum corneum (S), epidermis (E), and nail (N) are clearly delineated.

The 2D MEMS mirror was packaged with imaging optics in a compact aluminum housing to make a miniaturized OCT endoscope. Figure 34 illustrates the package design. The entire device measures < 6 mm in diameter and is compatible with requirements for minimally invasive endoscopic procedures. The housing can be machined for low cost and it allows precise adjustment of optical alignment using tiny set screws. The optics consists of a graded-index fiber collimator followed by an anti-reflection-coated achromat focusing lens that produces a beam diameter ($2w$) of ~ 13 μm . The mirror is mounted at 45 degrees and directs the beam orthogonal to the endoscope axis in a side-scanning configuration similar to those typically used for endoscopic OCT procedures. Post-objective scanning eliminates off-axis aberration encountered with pre-objective scanning. The 2D MEMS scanner can also be used for

endoscopic microscopy applications using fast-axis resonant scanning. Figure 35 shows the frequency response for the mirror. High-frequency scan rates up to 1.4 kHz are possible, which should enable real-time microscopy applications.

Preliminary *in vivo* imaging results of human skin were obtained with the MEMS endoscope (Figures 36). A modelocked Cr⁴⁺:Forsterite laser centered at 1250 nm with ~180 nm bandwidth was used to achieve 5 μ m axial resolutions. The transverse resolution was ~13 μ m. The stratum corneum, epidermis layer, and a spiraling sweat duct are visualized. Figure 36(b) shows an image of the human nailfold. Good delineation of the nailfold structure can be seen with low image speckle. Acquisition rates ranging from 2 Hz (1000 transverse pixels per image) to 20 Hz (160 transverse pixels per image) were demonstrated. Fast acquisition rates enabled real-time video capture and frame averaging in order to improve image contrast. These results are preliminary and were obtained with uncoated mirror optics. Further improvement in sensitivity should be possible with the next generation of devices.

Clinical Imaging using Optical Coherence Tomography

Ultrahigh Resolution OCT in Ophthalmology

OCT has been most widely investigated in ophthalmology, where it is now used as a standard diagnostic imaging method in the assessment of retinal diseases such as macular holes, age-related macular degeneration, glaucoma, and diabetic retinopathy [1, 78-81]. Since the introduction of commercial OCT instrumentation for retinal imaging in 1996 by Humphrey Instruments, now Carl Zeiss Meditec, OCT technology has undergone multiple generations of improvement. The introduction of the third generation commercial instrument, the StratusOCT, in 2002 achieved a four-fold increase in imaging speed compared to earlier instruments. The commercial ophthalmic StratusOCT system, with ~10 μ m axial image resolution, provides more detailed cross-sectional information on retinal pathology than any other ophthalmic diagnostic technique. This system is beginning to achieve widespread acceptance as a standard ophthalmic diagnostic tool and is rapidly becoming available in many ophthalmology clinics. However, the detection of many early changes associated with early disease can require a more accurate quantification of retinal structure than possible with standard resolution OCT.

Using the broad bandwidth of our ultrahigh resolution (UHR) OCT system, we can achieve axial resolutions <3 μ m in the retina [7], which corresponds to a factor of five-fold improvement when compared to OCT technology that uses conventional superluminescent diode sources. The signal-to-noise ratio for the system is ~95 dB. This system enables a significant improvement in the visualization of intraretinal structures for earlier diagnosis and more precise staging of pathology (Figure 37). Standard resolution StratusOCT can visualize major intraretinal morphology such as retinal nerve fiber layer, retinal pigment epithelium, the inner and outer plexiform layers, and the inner and outer nuclear layers. Ultrahigh resolution OCT offers an unprecedented axial resolution to visualize intraretinal morphology such as the external limiting membrane and the photoreceptor inner and outer segments. These intraretinal structures are relevant in a variety of retinal diseases, including age-related macular degeneration, diabetic retinopathy, and glaucoma (the three leading causes of blindness worldwide).

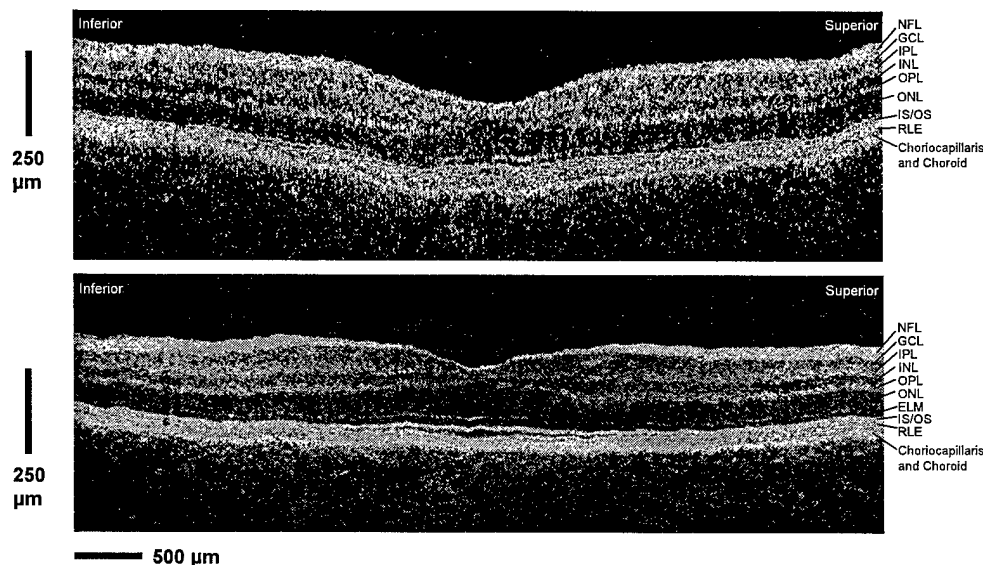


Figure 37. *In vivo* standard resolution OCT3 (top) and ultrahigh resolution (bottom) OCT images of a normal human fovea at approximately the same site. Resolutions were $\sim 10\text{-}15\text{ }\mu\text{m}$ (axial) $\times 15\text{ }\mu\text{m}$ (transverse) and $\sim 3\text{ }\mu\text{m}$ (axial) $\times 15\text{ }\mu\text{m}$ (transverse), respectively.

In addition to *in vivo* retinal imaging of normal subjects, we have begun clinical studies to compare the performance of the commercial StratusOCT instrument and the ultrahigh resolution OCT prototype for the retinal imaging of ophthalmology patients. We have developed a compact, low-threshold Ti:Sapphire laser that is robust and portable and can be used in the ophthalmology clinic [15]. The diagnosis of retinal pathology was performed using standard methods, including fundus examination, fundus photography, and/or fluorescein angiography.

A total of more than 700 patients have been imaged so far at the Tufts-New England Eye Center. Figure 38 illustrates OCT scans of a patient with macular hole Stage I. Ultrahigh resolution OCT provides unprecedented axial resolution to visualize the intraretinal morphology of retinal diseases. It promises to provide additional information that can be used to understand retinal disease morphology, pathogenesis, and management.

The visualization and quantification of retinal and intraretinal layers should serve as a valuable clinical tool for the early assessment of ophthalmic disease. We demonstrated this concept in a mouse retinal disease model, which allows us to follow and track different retinal diseases in this animal. Using the ultrahigh resolution OCT system, we have imaged and identified the many intraretinal layers of the mouse retina. Figure 39 illustrates the ability for ultrahigh resolution OCT to visualize the intraretinal layers of a normal mouse retina *in vivo*. When compared with histology taken from the same animal, the ultrahigh resolution OCT image corresponds well with the layers identified in the histology.

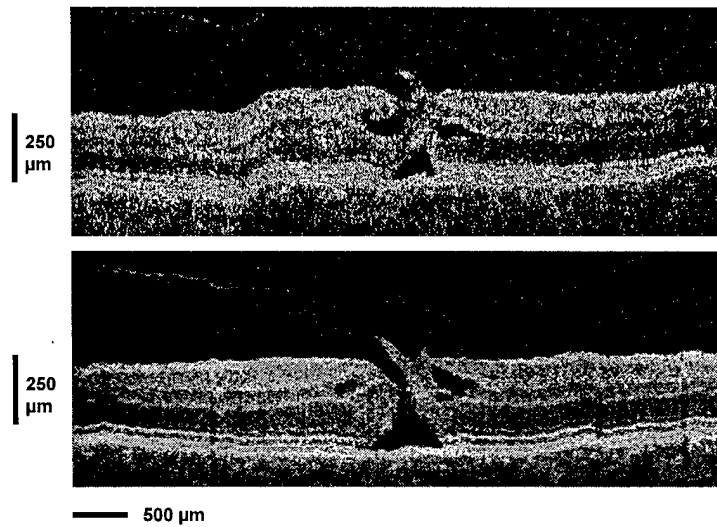


Figure 38. Standard resolution StratusOCT (top) and ultrahigh resolution (bottom) OCT images in a patient with stage I macular hole. Resolutions were $\sim 10\text{-}15\ \mu\text{m}$ (axial) $\times 15\ \mu\text{m}$ (transverse) and $\sim 3\ \mu\text{m}$ (axial) $\times 15\ \mu\text{m}$ (transverse), respectively.

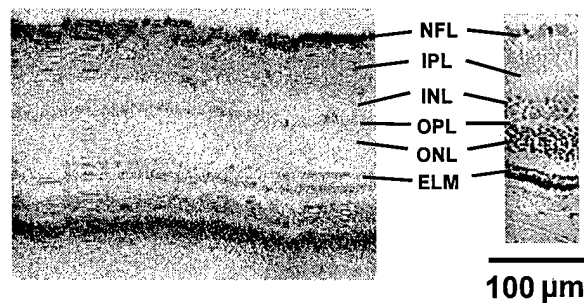


Figure 39. *In vivo* ultrahigh resolution OCT image of a normal mouse retina and its corresponding histology. The layers identified in the OCT images correspond well with histology.

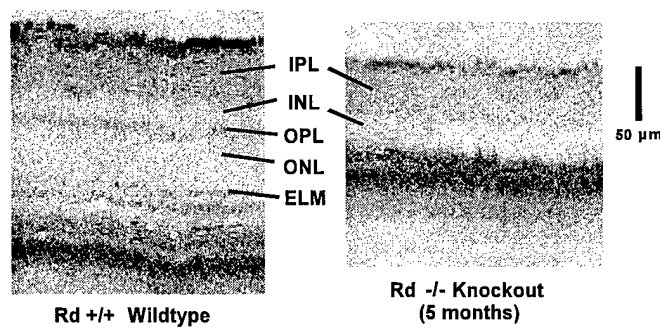


Figure 40. *In vivo* ultrahigh resolution OCT image of a normal mouse retina (Rd +/+ wild type) and a rhodopsin knockout mouse retina (Rd -/-). OCT has the ability to quantify the thickness of the different intraretinal layers as well as track disease progression.

In the rhodopsin knockout mouse, the outer plexiform and outer nuclear layers undergo degeneration three months postpartum. Figure 40 illustrates the differences between the *in vivo* OCT images of a normal mouse retina and a rhodopsin knockout mouse retina. At 5 months of age, the outer plexiform layer and the outer nuclear layer of the rhodopsin knockout mouse retina would have undergone degeneration. When comparing the knockout mouse retina with the normal wild-type mouse retina, the OCT image clearly demonstrates this degeneration in the knockout mouse. The *in vivo* ultrahigh resolution OCT images clearly depict the degeneration of the outer plexiform and the outer nuclear layer in the rhodopsin knockout mouse retina.

Ultrahigh Resolution and 3D Imaging of the Lower Gastrointestinal Tract *Ex Vivo*

Colorectal cancer (CRC) is a common and lethal disease. Approximately 148,000 new cases of large bowel cancer are diagnosed each year in the United States, and approximately one in three people who develop CRC die of this disease. CRC is the second leading cause of cancer death, accounting for 10- 11% of cancer deaths overall [82]. The majority of colon and rectal cancers are endoluminal adenocarcinomas that arise from the mucosa. Therefore, there is significant interest in the development of diagnostic techniques that can detect early stage colorectal disease.

Optical coherence tomography has the advantage of a higher resolution than current clinical ultrasound without the need for tissue contact or imaging through a transducing medium. Since OCT can be incorporated into a variety of endoscopic and laparoscopic imaging devices [30, 38], it has the particular advantage of enabling the visualization of microscopic mucosal and submucosal architectural features that are not visible by using clinically available imaging methods. Endoscopic OCT has also been shown to provide complementary information to endoscopic ultrasound for potential applications in the staging of endoscopic tumor resection [83]. Because of these advantages, there is significant interest in using OCT to improve current endoscopic diagnostic techniques for detecting early stage disease.

Working in collaboration with Dr. James Connolly from the Beth Israel Deaconess Medical Center, we are investigating imaging of gastrointestinal pathology using ultrahigh resolution OCT in the pathology laboratory. The goal of this study was to investigate the feasibility of using ultrahigh resolution OCT for imaging pathologies of the gastrointestinal tract *ex vivo* in order to provide a basis for interpreting future endoscopic OCT studies using ultrahigh resolution imaging. Advances in OCT technology have enabled the development of portable ultrahigh resolution, high-speed OCT technology, which has image resolutions of $<5\ \mu\text{m}$, a factor of two to three times finer than standard endoscopic OCT imaging systems. Imaging in the pathology laboratory allows access to fresh surgical specimens, control of imaging parameters, and accurate registration of OCT images with histology, which is difficult to achieve in *in vivo* OCT imaging. In order to preserve diagnostic integrity, specimens often cannot be removed from the hospital. The capability of performing ultrahigh resolution imaging in the pathology lab setting enables access to tissues that were previously inaccessible and is especially important as a research tool.

In this study, normal and pathologic areas from 22 surgical specimens of the gastrointestinal tract from adult patients were imaged. We used a novel compact solid-state Cr^{4+} :Forsterite laser operating at a center wavelength of 1260 nm as well as a compact nonlinear fiber source based

on a femtosecond Nd:Glass laser. This second source operated at a center wavelength of 1090 nm. Tissue scattering and absorption are minimized by using light in the near infrared (1200 to 1300 nm) range, thus permitting OCT imaging to be performed at 1-2 mm depths in most tissues. Using these laser light sources, it was possible to achieve an axial resolution of $\sim 3\text{-}5\text{ }\mu\text{m}$ in tissue, a factor of two to three times higher than standard endoscopic OCT systems previously used to image scattering tissues *in vivo*. The transverse image resolution was determined by the focused spot size of the optical beam, which is related to the numerical aperture of the focusing lens and the wavelength of the light source, as in conventional microscopy. We investigated imaging with transverse spot size of $18\text{ }\mu\text{m}$ using the Cr^{4+} :Forsterite laser system and $10\text{ }\mu\text{m}$ using the nonlinear fiber source. Imaging was performed by using a surgical imaging probe (measuring 1 cm in diameter and 15 cm in length) that was mounted on a precision stage to provide controlled displacements of the light beam orientation and position. Imaging was performed at 2-4 frames per second, enabling real-time visualization and the ability to adjust the imaging plane. Imaging was performed without contact with the tissue in order to prevent alterations in scattering and brightness due to the pressure of the probe on the tissue.

Studies were performed on freshly excised surgical specimens in the pathology laboratory of Beth Israel Deaconess Medical Center. Normal and diseased tissues from surgical resections were imaged within two hours of excision. Since the OCT source light was in the near infrared and invisible to the naked eye, tissue registration was performed with a visible green light guiding beam that was coincident with the OCT imaging beam. Specimens were marked at the beginning and end of each OCT scan with microinjections of ink to designate the orientation of the OCT imaging plane. Tissue specimens were then placed in 10% buffered formalin, routinely processed, and paraffin embedded. Multiple serial tissue sections of $5\text{ }\mu\text{m}$ thickness were obtained and stained with hematoxylin and eosin. Samples were sectioned in the same plane as the OCT imaging plane. Digital two-dimensional OCT images and histology sections corresponding to the imaged areas were compared. Minor discrepancies between histology and OCT imaging can be attributed to tissue fixation, processing, and sectioning artifacts.

Figure 41 shows normal colon specimens. OCT imaging of the normal colon produced distinct images of the mucosa, including the muscularis mucosa and submucosa characteristic of normal colonic microstructure. Full thickness mucosa of the colon is visible. High scattering bands as thin as $25\text{ }\mu\text{m}$, which corresponds to the muscularis mucosa, could be visualized in OCT images. This corresponds to what is seen in the histology; delineating the mucosa from the underlying stroma. The submucosa appears as a pale and less optically scattering layer. Figure 41(b) shows a higher magnification image where individual crypts are visible.

Images of chronic colitis due to ulcerative colitis and Crohn's disease are shown in Figures 42(a) and 42(b). Ulceration and erosion of the epithelium is evident. Irregular and distorted glands that are characteristic of chronic inflammatory bowel disease were clearly visible. In addition, the markedly increased inflammatory cells within the supporting lamina propria were noted and appeared as highly scattering. Figure 42(c) shows an image of invasive adenocarcinoma. Highly scattering and irregular invasive glands were visible in OCT images of adenocarcinoma. OCT images of invasive carcinoma revealed a complete loss of normal mucosal architecture and invasion of the submucosa. OCT images also identified areas within the carcinomas of ulceration with overlying fibrinopurulent exudate.

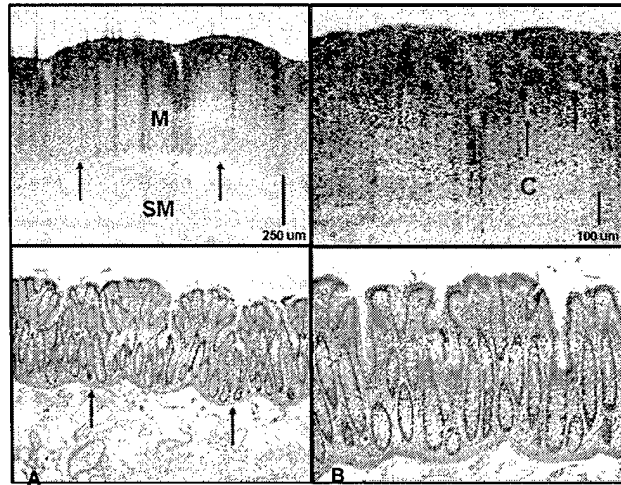


Figure 41. (a) OCT image of the normal colon acquired with the Cr^{4+} :Forsterite laser. Mucosa (M) is clearly delineated from underlying submucosa (SM) by a scattering band that corresponds to the thin muscularis mucosa (arrows). Mucosal folds and crypts are visible. The submucosa is shown as a loose and less optically scattering layer. (b) Higher magnification shows individual colonic crypts (arrows). (OCT top; histology bottom, H&E, A: 40x; B:100x)

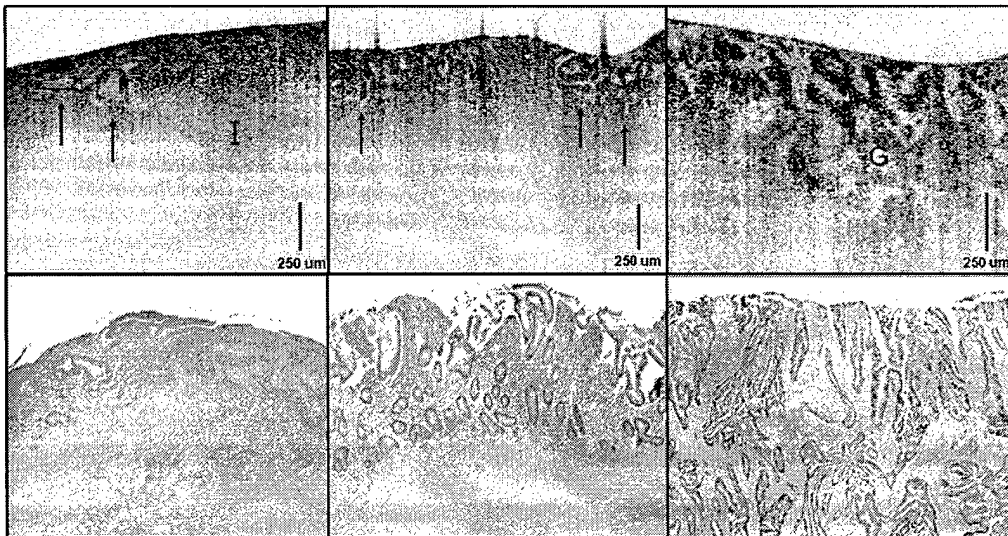


Figure 42. (a) OCT images with the Cr^{4+} :Forsterite laser of severe ulcerative colitis showing surface ulceration, architectural distortion of glands (arrows) and a dense chronic inflammatory infiltrate within the lamina propria (I). (b) Chronic colitis due to Crohn's disease showing branching irregular glands (arrows) and a dense inflammatory infiltrate in the lamina propria. (c) Well differentiated adenocarcinoma. Highly irregular invasive glands (G) are visible in a desmoplastic stroma. (top: OCT; bottom: histology, H&E; 40x)

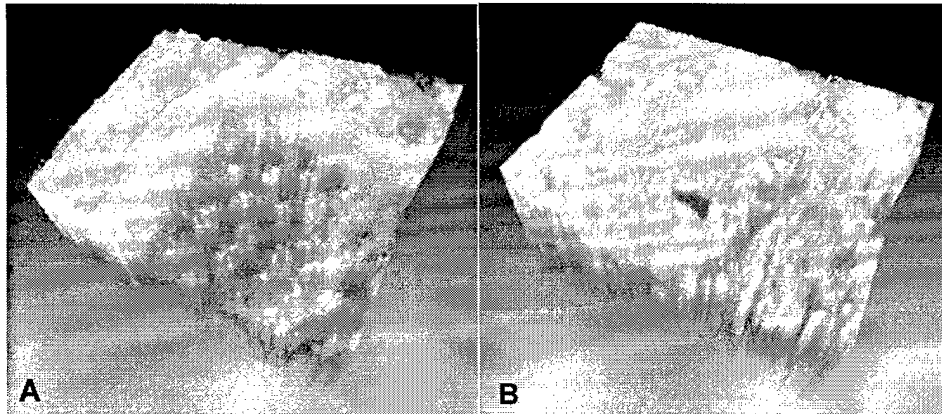


Figure 43. Volume rendering of (a) normal colon mucosa and (b) polypoid adenoma. Distinctive surface pattern and subsurface architecture were distinct for normal mucosa compared to adenoma. The rendered volumes are approximately 1 mm x 1 mm x 1.3 mm in dimension and consist of 200-300 transverse slices.

Volume rendering of colon mucosa is shown in Figure 43. Individual crypts which were difficult to identify in a single cross-sectional image could be confirmed based on their shape and distribution in the rendered en face plane. Folds in the mucosa could be clearly distinguished from crypts. It was also possible to render the surface of the epithelium. OCT images identified distinctive surface pit patterns in normal mucosa based on a view similar to that of magnification endoscopy. A volume rendering of the polypoid adenoma is shown in Figure 43(b). Both the surface pattern and subsurface architecture were distinct from that of normal colon mucosa. A comparison of cutaway en face views exposed dramatic irregular glandular structures in adenoma which were distinct from the relatively uniform crypt distribution in normal colon mucosa.

These preliminary results demonstrate the feasibility of ultrahigh resolution OCT imaging by using a portable system in a pathology laboratory environment. Ultrahigh resolution OCT clearly distinguished the epithelial layer of the mucosa and visualized individual villi, glands, and crypts. Inflammation and architectural distortion of glands due to inflammatory and malignant processes were observed. Visualization of submucosal lipoma was possible, as was invasion by squamous cell carcinoma and adenocarcinoma. Three-dimensional rendering enabled visualization of surface pit pattern and mucosal folds as well as subsurface microstructure. All OCT images showed strong correlations with architectural morphology in histological findings. Ultrahigh resolution OCT allows improved visualization of both normal and pathologic mucosal and submucosal morphology. This study supports using novel ultrahigh resolution OCT systems for imaging the lower gastrointestinal tract and provides a baseline for interpreting future ultrahigh resolution endoscopic OCT studies.

Endoscopic Imaging of Barrett's Esophagus and Gastrointestinal Cancer

Epithelial cancers of the gastrointestinal tract, reproductive tract, and the respiratory tract comprise the majority of cancers encountered in internal medicine. Many epithelial cancers are

preceded by pre-malignant changes, such as dysplasia. Conventional screening methods often rely on the gross morphological characteristics of tissues. Biopsy and histopathology are the standard for the diagnosis of dysplasia or carcinoma, but they can suffer from sampling errors and are cumbersome for screening and surveillance applications. Our hypothesis is that OCT can function as a form of "optical biopsy", which can perform microstructural imaging of tissue morphology *in situ* without excision. We have examined the use of OCT for the identification of early neoplastic changes and tissue abnormalities that have a predisposition to malignancy. Our group, as well as others, have performed investigations of *in vivo* endoscopic OCT imaging in human subjects [34, 84-86]. The aim of this work is to perform imaging of architectural morphology of the human upper gastrointestinal tract to explore the feasibility of ultrahigh resolution OCT for the identification of morphologies that are characteristic of early neoplastic changes.

The identification of early malignant changes remains a central objective of clinical medicine since, once widely metastatic, most neoplasms become incurable. In addition to biochemical methods, excisional biopsy, with subsequent histologic processing, remains a cornerstone of early diagnostics. However, in many instances, diagnostics based on excisional biopsy are ineffective because of sampling errors. A technology capable of performing optical biopsy (i.e., imaging at a resolution comparable to histopathology without the need for tissue removal) could significantly improve the ability of clinicians to identify malignancies at curable stages [87-91]. Large areas could be screened in real time with an imaging system that is high resolution and relatively low cost. High-resolution imaging of architectural morphology may allow the *in situ* assessment of early neoplastic changes such as dysplasia. If successful, this technology could be coupled with excisional biopsy in order to reduce sampling errors and false-negative rates. We have investigated the feasibility of optical biopsy with OCT to identify early neoplastic changes. Although we believe that micron-scale imaging has the potential to be a general diagnostic in most, if not all, organ systems, this study will emphasize one clinical scenario where current methods of excisional screening are plagued with serious limitations: the problem of early neoplastic diagnosis in Barrett's esophagus.

Barrett's esophagus is the replacement of the squamous epithelium of the distal esophagus with columnar epithelium [92]. It is believed to be caused by chronic gastroesophageal reflux. Several well-designed studies have demonstrated that Barrett's esophagus is associated with a 30-40x increased risk of developing adenocarcinoma. The prevalence of Barrett's esophagus within the US population is between 0.3% and 2% [93]. Among patients with reflux, the prevalence is 8-14% [94, 95]. The incidence of progression to adenocarcinoma in Barrett's esophagus is approximately 7-9% [96]. For this reason, endoscopic surveillance of Barrett's epithelium every 6-18 months is recommended. Endoscopic screening currently involves random biopsies every 2 cm. However, sampling errors exist and may miss small foci of carcinoma [97, 98]. Because of the imprecision and high cost associated with screening, new methods are required to identify high risk patients.

An important technology that is necessary in order to apply OCT to the imaging of internal organ systems is a catheter-endoscope, which is capable of delivering, focusing, scanning, and collecting a single spatial mode optical beam. We have developed, tested, and applied a prototype transverse scanning OCT catheter that is suitable for luminal imaging [99]. The OCT

catheter consists of an optical coupling element at its proximal end, a single-mode fiber running the length of the catheter, and optical focusing and beam directing elements at the distal end. The catheter is designed to scan the beam in a circumferential or longitudinal pattern in order to cross-sectionally image through the lumen (or other biological structures) into which it is inserted. A single-mode optical fiber lies within a flexible speedometer cable that is rotated with a motor drive unit at the proximal end. The distal end contains a graded index (GRIN) lens to focus the imaging beam and a right-angle micropism to direct the beam at a 90-degree angle with respect to the axis of the catheter. The entire assembly is housed in a transparent plastic sheath that can be disinfected prior to use and is discarded after use.

The development and application of OCT has been made possible by the vertically integrated structure of our research program at the Massachusetts Institute of Technology, which combines fundamental physical studies, engineering, biomedical studies, and clinical applications. In order to achieve the high powers and short coherence lengths necessary for high resolution, high speed imaging, a Cr:Forsterite laser is used as the light source. This laser generates short pulses in the 1200-1350 nm wavelength regime. The Cr:Forsterite laser has a coherence length of 15 microns. However, because it generates short pulses, the output bandwidth can be increased by using nonlinear effects in optical fibers to yield coherence lengths of 5 microns or less. Nonlinear techniques such as these are well established in laser engineering and research, and they have been used for many applications including pulse compression and signal processing [44, 46, 100, 101].

This study is performed in collaboration with Dr. Hiroshi Mashimo at the Veterans Affairs Medical Center of the Boston Healthcare system to perform ultrahigh resolution OCT imaging of patients who are diagnosed with Barrett's esophagus and who have a predisposition to the presence of dysplasia or adenocarcinoma of the esophagus. Figure 44 shows an example OCT image of an abnormal esophageal region and an endoscopic video image of the area. The video image reveals both normal regions of the esophagus and finger-like projections of abnormal epithelium that are indicative of Barrett's esophagus. Figure 45(a) shows an OCT image of normal columnar epithelium in the stomach in the same patient. Pit architecture within the gastric (gp) is visible as regular vertical regions of high backscattering intensity. Small pockets of mucosal secretion below the surface are also visualized as weakly scattering regions that are circular in geometry and have approximate diameters of 50-100 μm . Figure 45(b) shows an OCT image of normal esophagus with squamous epithelium. The OCT image illustrates the relatively homogeneous epithelium (ep), the high-backscattering region (appears brighter) of the lamina propria (lp), the low-backscattering muscularis mucosa (mm), the high-backscattering submucosa (sm), and the low-backscattering and thick muscularis propria (mp). The solid horizontal line noted above the mucosal surface is from the transparent plastic sheath of the OCT catheter. The OCT images show clear differences in the tissue architecture of the Barrett's region in Figure 44 when compared to squamous epithelium of normal esophagus in Figure 45(b). The uniformly layered structure of normal esophagus is disrupted by the presence of multiple crypt- and gland-like structures and is highly heterogeneous.

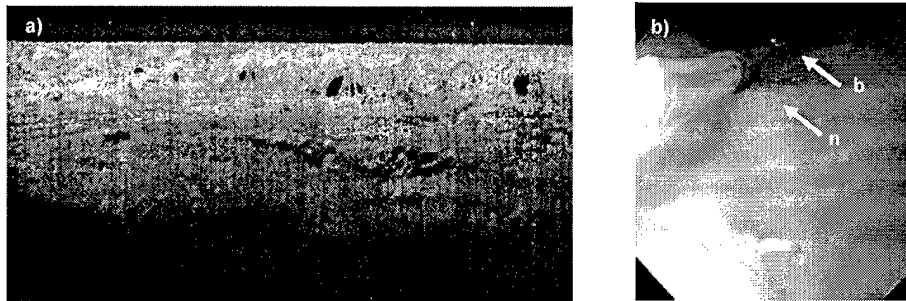


Figure 44. (a) Ultrahigh resolution OCT image of Barrett's esophagus. Architectural disruption and glandular features are highly distinct and can be differentiated well from OCT images of the normal esophagus. (b) Endoscopic view of a patient's esophagus and the OCT catheter. Regions of Barrett's esophagus 'b' are seen as finger-like projections consisting of a darker hue than the normal pink esophageal tissue 'n'. The red aiming beam of the OCT catheter is also visible, which indicates the area being imaged.

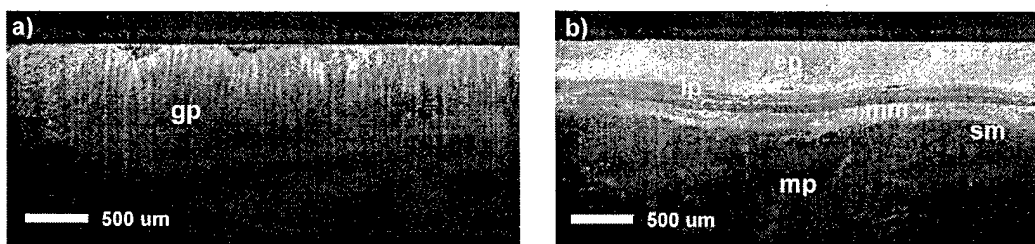


Figure 45. (a) Ultrahigh resolution OCT image of gastric mucosa. Gastic pits (gp) are clearly visible as vertical regions of high backscattering (bright) intensity. (b) Ultrahigh resolution OCT image of normal esophagus. Layered structure of the esophagus is well defined with a homogeneous epithelium (ep) above a highly backscattering lamina propria (lp). Deeper layers of the muscularis mucosa (mm), submucosa (sm), and muscularis propria (mp) are also visualized.

OCT enables the visualization of architectural morphology features, such as the normal, layered structure of the epithelium, as opposed to the glandular and crypt structures associated with Barrett's esophagus. Because pinch biopsies were obtained, it was not possible to exactly orient the sectioning plane of the histology, as with *in vitro* imaging studies. The correspondence of OCT with histology was evaluated, based on the presence or absence of architectural morphology, which indicates normal as opposed to Barrett's esophagus.

It has been demonstrated that endoscopic OCT resolution can differentiate between normal and Barrett's epithelium in real-time, based on differences in epithelial architecture. Crypt-like and gland-like structures that disrupted the relatively uniform layers of squamous epithelium are readily identified, thus enabling the differentiation between normal and Barrett's epithelium.

The ability to differentiate between normal and Barrett's epithelium suggests that the OCT could be used for screening applications. These findings are consistent with other investigations [34, 84-86]. In the surveillance of patients with Barrett's esophagus for high-grade dysplasia and adenocarcinoma, the most intriguing application of OCT would be to direct excisional biopsy in order to reduce sampling errors. Developing this application requires detailed investigation imaging larger numbers of patients with high grade dysplasia and evaluating correlations with histology. These studies are currently in process. If successfully, one can envision new OCT imaging probes that integrate OCT imaging with pinch biopsy in order to provide a real-time "first look" at pathology prior to the excision and processing of a specimen. If successful, this technology could be used to help guide excision biopsy in order to reduce sampling errors and false-negative rates. This could improve the sensitivity of diagnosis, reduce the cost of surveillance, and provide enhanced diagnosis and treatment decisions.

References

- [1] D. Huang, E. A. Swanson, C. P. Lin, J. S. Schuman, W. G. Stinson, W. Chang, M. R. Hee, T. Flotte, K. Gregory, C. A. Puliafito, and J. G. Fujimoto, "Optical coherence tomography," *Science*, vol. 254, pp. 1178-81, 1991.
- [2] J. G. Fujimoto, "Optical coherence tomography for ultrahigh resolution in vivo imaging," *Nature biotechnology*, vol. 21, pp. 1361-7, 2003.
- [3] J. G. Fujimoto, M. E. Brezinski, G. J. Tearney, S. A. Boppart, B. Bouma, M. R. Hee, J. F. Southern, and E. A. Swanson, "Optical biopsy and imaging using optical coherence tomography," *Nature medicine*, vol. 1, pp. 970-2, 1995.
- [4] M. Brezinski, G. Tearney, B. Bouma, J. Izatt, M. Hee, E. Swanson, J. Southern, and J. Fujimoto, "Optical coherence tomography for optical biopsy: properties and demonstration of vascular pathology," *Circulation*, vol. 93, pp. 1206-13, 1996.
- [5] J. G. Fujimoto, C. Pitris, S. A. Boppart, and M. E. Brezinski, "Optical coherence tomography: an emerging technology for biomedical imaging and optical biopsy," *Neoplasia*, vol. 2, pp. 9-25, 2000.
- [6] W. Drexler, U. Morgner, R. K. Ghanta, F. X. Kaertner, J. S. Schuman, and J. G. Fujimoto, "Ultrahigh resolution ophthalmic optical coherence tomography," *Nature Medicine*, vol. 7, pp. 502-507, 2001.
- [7] W. Drexler, U. Morgner, F. X. Kartner, C. Pitris, S. A. Boppart, X. D. Li, E. P. Ippen, and J. G. Fujimoto, "In vivo ultrahigh-resolution optical coherence tomography," *Optics Letters*, vol. 24, pp. 1221-3, 1999.
- [8] B. E. Bouma, G. J. Tearney, I. P. Bilinsky, and B. Golubovic, "Self phase modulated Kerr-lens mode locked Cr:forsterite laser source for optical coherence tomography," *Optics Letters*, vol. 21, pp. 1839-1841, 1996.
- [9] J. K. Ranka, R. S. Windeler, and A. J. Stentz, "Visible continuum generation in air-silica microstructure optical fibers with anomalous dispersion at 800 nm," *Optics Letters*, vol. 25, pp. 25-7, 2000.
- [10] T. Birks, W. Wadsworth, and P. S. J. Russell, "Supercontinuum generation in tapered fibers," *Optics Letters*, vol. 25, pp. 1415-1417, 2000.
- [11] I. Hartl, X. D. Li, C. Chudoba, R. K. Ghanta, T. H. Ko, J. G. Fujimoto, J. K. Ranka, and R. S. Windeler, "Ultrahigh-resolution optical coherence tomography using continuum generation in an air-silica microstructure optical fiber," *Optics Letters*, vol. 26, pp. 608-610, 2001.
- [12] B. E. Bouma, G. J. Tearney, S. A. Boppart, M. R. Hee, M. E. Brezinski, and J. G. Fujimoto, "High-resolution optical coherence tomographic imaging using a mode-locked Ti:Al₂O₃ laser source," *Optics Letters*, vol. 20, pp. 1486-1488, 1995.
- [13] B. Povazay, K. Bizheva, A. Unterhuber, B. Hermann, H. Sattmann, A. F. Fercher, W. Drexler, A. Apolonski, W. J. Wadsworth, J. C. Knight, P. S. J. Russell, M. Vetterlein, and E. Scherzer, "Submicrometer axial resolution optical coherence tomography," *Optics Letters*, vol. 27, pp. 1800-2, 2002.
- [14] Y. Wang, Y. Zhao, J. S. Nelson, Z. Chen, and R. S. Windeler, "Ultrahigh-resolution optical coherence tomography by broadband continuum generation from a photonic crystal fiber," *Optics Letters*, vol. 28, pp. 182-4, 2003.
- [15] A. M. Kowalewicz, T. R. Schibli, F. X. Kartner, and J. G. Fujimoto, "Ultralow-threshold Kerr-lens mode-locked Ti:Al₂O₃ laser," *Optics Letters*, vol. 27, pp. 2037-2039, 2002.

- [16] A. Unterhuber, B. Povazay, B. Hermann, H. Sattmann, W. Drexler, V. Yakovlev, G. Tempea, C. Schubert, E. M. Anger, P. K. Ahnelt, M. Stur, J. E. Morgan, A. Cowey, G. Jung, T. Le, and A. Stingl, "Compact, low-cost Ti:Al₂O₃ laser for in vivo ultrahigh-resolution optical coherence tomography," *Optics letters*, vol. 28, pp. 905-7, 2003.
- [17] J. M. Schmitt, A. Knüttel, M. Yadlowsky, and M. A. Eckhaus, "Optical coherence tomography of a dense tissue - statistics of attenuation and backscattering," *Physics in Medicine and Biology*, vol. 39, pp. 1705-1720, 1994.
- [18] B. E. Bouma, G. J. Tearney, I. P. Bilinsky, B. Golubovic, and J. G. Fujimoto, "Self-phase-modulated Kerr-lens mode-locked Cr:forsterite laser source for optical coherence tomography," *Optics Letters*, vol. 21, pp. 1839-41, 1996.
- [19] K. Bizheva, B. Povazay, B. Hermann, H. Sattmann, W. Drexler, M. Mei, R. Holzwarth, T. Hoelzenbein, V. Wacheck, and H. Pehamberger, "Compact, broad-bandwidth fiber laser for sub-2-microm axial resolution optical coherence tomography in the 1300-nm wavelength region," *Optics letters*, vol. 28, pp. 707-9, 2003.
- [20] S. Bourquin, A. D. Aguirre, I. Hartl, P. Hsiung, T. H. Ko, and J. G. Fujimoto, "Compact broadband light source for ultra high resolution optical coherence tomography imaging using a femtosecond Nd:Glass laser and a nonlinear fiber," *Optics Express*, vol. 11, pp. 3290-3297, 2003.
- [21] K. L. Corwin, N. R. Newbury, J. M. Dudley, S. Coen, S. A. Diddams, K. Weber, and R. S. Windeler, "Fundamental noise limitations to supercontinuum generation in microstructure fiber," *Physical Review Letters*, vol. 90, pp. 113904-1, 2003.
- [22] P. A. Champert, S. V. Popov, and J. R. Taylor, "Generation of multiwatt, broadband continua in holey fibers," *Optics Letters*, vol. 27, pp. 122-4, 2002.
- [23] L. Provino, J. M. Dudley, H. Maillotte, N. Grossard, R. S. Windeler, and B. J. Eggleton, "Compact broadband continuum source based on microchip laser pumped microstructured fibre," *Electronics Letters*, vol. 37, pp. 558-60, 2001.
- [24] A. V. Avdokhin, S. V. Popov, and J. R. Taylor, "Continuous-wave, high-power, in Raman continuum generation holey fibers," *Optics Letters*, vol. 28, pp. 1353-1355, 2003.
- [25] N. Nishizawa and T. Goto, "Widely broadened supercontinuum generation using highly nonlinear dispersion shifted fibers and femtosecond fiber laser," *Jpn. J. Appl. Phys.*, vol. 40, pp. 365-367, 2001.
- [26] J. W. Nicholson, M. F. Yan, P. Wisk, J. Fleming, F. DiMarcello, E. Monberg, A. Yablon, C. Jorgensen, and T. Veng, "All-fiber, octave-spanning supercontinuum," *Optics Letters*, vol. 28, pp. 643-645, 2003.
- [27] B. E. Bouma, L. E. Nelson, G. J. Tearney, D. J. Jones, M. E. Brezinski, and J. G. Fujimoto, "Optical coherence tomographic imaging of human tissue at 1.55 μ m and 1.81 μ m using Er and Tm-doped fiber sources," *Journal of Biomedical Optics*, vol. 3, pp. 76-9, 1998.
- [28] J. M. Schmitt, S. H. Xiang, and K. M. Yung, "Differential absorption imaging with optical coherence tomography," *Journal of the Optical Society of America A (Optics, Image Science and Vision)*, vol. 15, pp. 2288-96, 1998.
- [29] P. R. Pfau and M. V. Sivak, Jr., "Endoscopic diagnostics," *Gastroenterology*, vol. 120, pp. 763-781, 2001.
- [30] A. M. Sergeev, V. M. Gelikonov, G. V. Gelikonov, F. I. Feldchtein, R. V. Kuranov, N. D. Gladkova, N. M. Shakhova, L. B. Snopova, A. V. Shakov, I. A. Kuznetzova, A. N. Denisenko, V. V. Pochinko, Y. P. Chumakov, and O. S. Streltsova, "In vivo endoscopic

- OCT imaging of precancer and cancer states of human mucosa," *Optics Express*, vol. 1, pp. 432, 1997.
- [31] S. Jäckle, N. Gladkova, F. Feldchtein, A. Terentieva, B. Brand, G. Gelikonov, V. Gelikonov, A. Sergeev, A. Fritscher-Ravens, J. Freund, U. Seitz, S. Schröder, and N. Soehendra, "In vivo endoscopic optical coherence tomography of esophagitis, Barrett's esophagus, and adenocarcinoma of the esophagus," *Endoscopy*, vol. 32, pp. 750-5, 2000.
 - [32] M. V. Sivak, K. Kobayashi, J. A. Izatt, A. M. Rollins, R. Ung-runyawee, A. Chak, R. C. K. Wong, G. A. Isenberg, and J. Willis, "High-resolution endoscopic imaging of the GI tract using optical coherence tomography," *Gastrointestinal Endoscopy*, vol. 51, pp. 474-479, 2000.
 - [33] B. E. Bouma, G. J. Tearney, C. C. Compton, and N. S. Nishioka, "High-resolution imaging of the human esophagus and stomach in vivo using optical coherence tomography," *Gastrointestinal endoscopy*, vol. 51(4) Pt 1, pp. 467-74, 2000.
 - [34] X. D. Li, S. A. Boppart, J. Van Dam, H. Mashimo, M. Mutinga, W. Drexler, M. Klein, C. Pitris, M. L. Krinsky, M. E. Brezinski, and J. G. Fujimoto, "Optical coherence tomography: advanced technology for the endoscopic imaging of Barrett's esophagus," *Endoscopy*, vol. 32, pp. 921-30, 2000.
 - [35] J. M. Poneros, S. Brand, B. E. Bouma, G. J. Tearney, C. C. Compton, and N. S. Nishioka, "Diagnosis of specialized intestinal metaplasia by optical coherence tomography," *Gastroenterology*, vol. 120, pp. 7-12, 2001.
 - [36] P. R. Pfau, M. V. Sivak, A. Chak, M. Kinnard, R. C. K. Wong, G. A. Isenberg, J. A. Izatt, A. Rollins, and V. Westphal, "Criteria for the diagnosis of dysplasia by endoscopic optical coherence tomography," *Gastrointestinal Endoscopy*, vol. 58, pp. 196-202, 2003.
 - [37] F. X. Kartner, N. Matuschek, T. Schibli, U. Keller, H. A. Haus, C. Heine, R. Morf, V. Scheuer, M. Tilsch, and T. Tschudi, "Design and fabrication of double-chirped mirrors," *Optics Letters*, vol. 22, pp. 831-833, 1997.
 - [38] G. J. Tearney, M. E. Brezinski, B. E. Bouma, S. A. Boppart, C. Pitvis, J. F. Southern, and J. G. Fujimoto, "In vivo endoscopic optical biopsy with optical coherence tomography," *Science*, vol. 276, pp. 2037-9, 1997.
 - [39] F. Koenig, J. Knittel, and H. Stepp, "Diagnosing cancer in vivo," *Science*, vol. 292, pp. 1401-3, 2001.
 - [40] J. A. Izatt, M. R. Hee, G. M. Owen, E. A. Swanson, and J. G. Fujimoto, "Optical coherence microscopy in scattering media," *Optics Letters*, vol. 19, pp. 590-2, 1994.
 - [41] M. Kempe, W. Rudolph, and E. Welsch, "Comparative study of confocal and heterodyne microscopy for imaging through scattering media," *Journal of the Optical Society of America a-Optics Image Science and Vision*, vol. 13, pp. 46-52, 1996.
 - [42] M. Kempe and W. Rudolph, "Analysis of heterodyne and confocal microscopy for illumination with broad-bandwidth light," *Journal of Modern Optics*, vol. 43, pp. 2189-2204, 1996.
 - [43] A. D. Aguirre, P. Hsiung, T. H. Ko, I. Hartl, and J. G. Fujimoto, "High-resolution optical coherence microscopy for high-speed, in vivo cellular imaging," *Opt Lett*, vol. 28, pp. 2064-6, 2003.
 - [44] G. J. Tearney, B. E. Bouma, and J. G. Fujimoto, "High-speed phase- and group-delay scanning with a grating-based phase control delay line," *Optics Letters*, vol. 22, pp. 1811-13, 1997.

- [45] A. V. Zvyagin and D. D. Sampson, "Achromatic optical phase shifter-modulator," *Optics Letters*, vol. 26, pp. 187-189, 2001.
- [46] J. P. Heritage, A. M. Weiner, and R. N. Thurston, "Picosecond Pulse Shaping by Spectral Phase and Amplitude Manipulation," *Optics Letters*, vol. 10, pp. 609-611, 1985.
- [47] B. E. Lemoff and C. P. J. Barty, "Quintic-Phase-Limited, Spatially Uniform Expansion and Recompression of Ultrashort Optical Pulses," *Optics Letters*, vol. 18, pp. 1651-1653, 1993.
- [48] M. D. Kulkarni and J. A. Izatt, "Spectroscopic optical coherence tomography," *CLEO '96. Summaries of Papers Presented at the Conference on Lasers and Electro Optics*, vol. 9, pp. 59-60, 1996.
- [49] U. S. Sathyam, B. W. Colston, Jr., L. B. Da Silva, and M. J. Everett, "Evaluation of optical coherence quantitation of analytes in turbid media by use of two wavelengths," *Applied Optics*, vol. 38, pp. 2097-104, 1999.
- [50] L. T. Perelman, V. Backman, M. Wallace, G. Zonios, R. Manoharan, A. Nusrat, S. Shields, M. Seiler, C. Lima, T. Hamano, I. Itzkan, J. Van Dam, J. M. Crawford, and M. S. Feld, "Observation of periodic fine structure in reflectance from biological tissue: a new technique for measuring nuclear size distribution," *Physical Review Letters*, vol. 80, pp. 627-630, 1998.
- [51] V. Backman, R. Gurjar, K. Badizadegan, I. Itzkan, R. R. Dasari, L. T. Perelman, and M. S. Feld, "Polarized light scattering spectroscopy for quantitative measurement of epithelial cellular structures in situ," *IEEE Journal of Selected Topics in Quantum Electronics*, vol. 5, pp. 1019-26, 1999.
- [52] V. Backman, M. Wallace, L. T. Perelman, J. Arendt, R. Gurjar, M. Muller, Q. Zhang, G. Zonios, E. Kline, T. McGillican, S. Shapshay, T. Valdez, K. Badizadegan, J. M. Crawford, M. Fitzmaurice, S. Kabani, H. Levin, M. Seiler, R. R. Dasari, I. Itzkan, J. Van Dam, and M. S. Feld, "Detection of preinvasive cancer cells," *Nature*, vol. 406, pp. 35-36, 2000.
- [53] M. B. Wallace, L. T. Perelman, V. Backman, J. M. Crawford, M. Fitzmaurice, M. Seiler, K. Badizadegan, S. J. Shields, I. Itzkan, R. R. Dasari, J. Van Dam, and M. S. Feld, "Endoscopic detection of dysplasia in patients with Barrett's esophagus using light-scattering spectroscopy," *Gastroenterology*, vol. 119, pp. 677-682, 2000.
- [54] V. Backman, V. Gopal, M. Kalashnikov, K. Badizadegan, R. Gurjar, A. Wax, I. Georgakoudi, M. Mueller, C. W. Boone, R. R. Dasari, and M. S. Feld, "Measuring cellular structure at submicrometer scale with light scattering spectroscopy," *IEEE Journal of Selected Topics in Quantum Electronics*, vol. 7, pp. 887-93, 2001.
- [55] R. Gurjar, V. Backman, K. Badizadegan, R. R. Dasari, I. Itzkan, L. T. Perelman, and M. S. Feld, "Imaging human epithelial properties with polarized light scattering spectroscopy," *Nature medicine*, vol. 7, pp. 1245-1248, 2001.
- [56] A. Wax, C. Yang, V. Backman, M. Kalashnikov, R. Dasari, and M. S. Feld, "Determination of particle size by using the angular distribution of backscattered light as measured with low-coherence interferometry," *Journal of the Optical Society of America A*, vol. 19, pp. 737-744, 2002.
- [57] A. Wax, C. Yang, and J. A. Izatt, "Fourier-domain low-coherence interferometry for light-scattering spectroscopy," *Opt Lett*, vol. 28, pp. 1230-2, 2003.

- [58] J. Beuthan, O. Minet, J. Helfmann, M. Herrig, and G. Muller, "The spatial variation of the refractive index in biological cells," *Physics in Medicine and Biology*, vol. 41, pp. 369-382, 1996.
- [59] P. Sloot, A. Hoekstra, and C. Figdor, "Osmotic response of lymphocytes measured by means of forward light scattering: theoretical considerations," *Cytometry*, vol. 9, pp. 636-641, 1988.
- [60] W. Drexler, H. Sattmann, B. Hermann, T. H. Ko, M. Stur, A. Unterhuber, C. Scholda, O. Findl, M. Wirtitsch, J. G. Fujimoto, and A. F. Fercher, "Enhanced visualization of macular pathology with the use of ultrahigh-resolution optical coherence tomography," *Archives of ophthalmology*, vol. 121, pp. 695-706, 2003.
- [61] J. F. de Boer, B. Cense, B. H. Park, M. C. Pierce, G. J. Tearney, and B. E. Bouma, "Improved signal-to-noise ratio in spectral-domain compared with time-domain optical coherence tomography," *Opt Lett*, vol. 28, pp. 2067-9, 2003.
- [62] R. Leitgeb, C. K. Hitzenberger, and A. F. Fercher, "Performance of Fourier domain vs. time domain optical coherence tomography," *Optics Express*, vol. 11, 2003.
- [63] M. A. Choma, M. V. Sarunic, C. H. Yang, and J. A. Izatt, "Sensitivity advantage of swept source and Fourier domain optical coherence tomography," *Optics Express*, vol. 11, pp. 2183-2189, 2003.
- [64] R. A. Leitgeb, L. Schmetterer, W. Drexler, A. F. Fercher, R. J. Zawadzki, and T. Bajraszewski, "Real-time assessment of retinal blood flow with ultrafast acquisition by color Doppler Fourier domain optical coherence tomography," *Optics Express*, vol. 11, pp. 3116-3121, 2003.
- [65] R. Leitgeb, M. Wojtkowski, A. Kowalczyk, C. K. Hitzenberger, M. Sticker, and A. F. Fercher, "Spectral measurement of absorption by spectroscopic frequency-domain optical coherence tomography," *Optics Letters*, vol. 25, pp. 820-2, 2000.
- [66] M. Wojtkowski, V. J. Srinivasan, T. H. Ko, J. G. Fujimoto, A. Kowalczyk, and J. S. Duker, "Ultrahigh resolution, high speed, Fourier domain optical coherence tomography and methods for dispersion compensation," *Optics Express*, accepted.
- [67] M. Wojtkowski, A. Kowalczyk, R. Leitgeb, and A. F. Fercher, "Full range complex spectral optical coherence tomography technique in eye imaging," *Optics Letters*, vol. 27, pp. 1415-17, 2002.
- [68] M. Wojtkowski, R. Leitgeb, A. Kowalczyk, T. Bajraszewski, and A. F. Fercher, "In vivo human retinal imaging by Fourier domain optical coherence tomography," *Journal of Biomedical Optics*, vol. 7, pp. 457-63, 2002.
- [69] M. Wojtkowski, T. Bajraszewski, P. Targowski, and A. Kowalczyk, "Real-time in vivo imaging by high-speed spectral optical coherence tomography," *Opt Lett*, vol. 28, pp. 1745-7, 2003.
- [70] N. Nassif, B. Cense, B. H. Park, S. H. Yun, T. C. Chen, B. E. Bouma, G. J. Tearney, and J. F. de Boer, "In vivo human retinal imaging by ultrahigh-speed spectral domain optical coherence tomography," *Optics Letters*, vol. 29, pp. 480-482, 2004.
- [71] U. Morgner, F. X. Kartner, S. H. Cho, Y. Chen, H. A. Haus, J. G. Fujimoto, E. P. Ippen, V. Scheuer, G. Angelow, and T. Tschudi, "Sub-two-cycle pulses from a Kerr-lens mode-locked Ti:sapphire laser," *Optics Letters*, vol. 24, pp. 411-413, 1999.
- [72] Y. Pan, H. Xie, and G. K. Fedder, "Endoscopic optical coherence tomography based on a microelectromechanical mirror," *Optics Letters*, vol. 26, pp. 1966-8, 2001.

- [73] J. M. Zara, S. Yazdanfar, K. D. Rao, J. A. Izatt, and S. W. Smith, "Electrostatic micromachine scanning mirror for optical coherence tomography," *Optics letters*, vol. 28, pp. 628-30, 2003.
- [74] D. L. Dickensheets and G. S. Kino, "Micromachined scanning confocal optical microscope," *Optics Letters*, vol. 21, pp. 764-766, 1996.
- [75] W. Piyawattanametha, H. Toshiyoshi, L. LaCrosse, and M. C. Wu, "Surface-micromachined confocal scanning optical microscope," presented at Conference on Lasers and Electro-Optics (CLEO 2000), San Francisco, CA, USA, 2000.
- [76] L. Fan and M. C. Wu, "Two-dimensional optical scanner with large angle rotation realized by self-assembled micro-elevator," presented at IEEE LEOS Summer Topical Meeting on Optical MEMS, Monterey, CA, 1998.
- [77] W. Piyawattanametha, P. R. Patterson, D. Hah, H. Toshiyoshi, and M. C. Wu, "A 2D scanner by surface and bulk micromachined angular vertical comb actuators," presented at IEEE/LEOS International Conference on Optical MEMS, HI, USA, 2003.
- [78] M. R. Hee, J. A. Izatt, E. A. Swanson, D. Huang, C. P. Lin, J. S. Schuman, C. A. Puliafito, and J. G. Fujimoto, "Optical coherence tomography of the human retina," *Archives of Ophthalmology*, vol. 113, pp. 325-332, 1995.
- [79] C. A. Puliafito, M. R. Hee, J. S. Schuman, and J. G. Fujimoto, *Optical coherence tomography of ocular diseases*. Thorofare, NJ: Slack Inc., 1996.
- [80] C. A. Puliafito, M. R. Hee, C. P. Lin, E. Reichel, J. S. Schuman, J. S. Duker, J. A. Izatt, E. A. Swanson, and J. G. Fujimoto, "Imaging of macular diseases with optical coherence tomography," *Ophthalmology*, vol. 102, pp. 217-29, 1995.
- [81] J. S. Schuman, M. R. Hee, C. A. Puliafito, C. Wong, T. Pedut-Kloizman, C. P. Lin, E. Hertzmark, J. A. Izatt, E. A. Swanson, and J. G. Fujimoto, "Quantification of nerve fiber layer thickness in normal and glaucomatous eyes using optical coherence tomography," *Archives of ophthalmology*, vol. 113, pp. 586-96, 1995.
- [82] A. Jemal, R. C. Tiwari, T. Murray, A. Ghafoor, A. Samuels, E. Ward, E. J. Feuer, and M. J. Thun, "Cancer statistics, 2004," *CA Cancer J Clin*, vol. 54, pp. 8-29, 2004.
- [83] A. Das, M. V. Sivak, Jr., A. Chak, R. C. Wong, V. Westphal, A. M. Rollins, J. Willis, G. Isenberg, and J. A. Izatt, "High-resolution endoscopic imaging of the GI tract: a comparative study of optical coherence tomography versus high-frequency catheter probe EUS," *Gastrointestinal endoscopy*, vol. 54, pp. 219-24, 2001.
- [84] S. Brand, J. M. Poneros, B. E. Bouma, G. J. Tearney, C. C. Compton, and N. S. Nishioka, "Optical coherence tomography in the gastrointestinal tract," *Endoscopy*, vol. 32, pp. 796-803, 2000.
- [85] G. Zuccaro, N. Gladkova, J. Vargo, F. Feldchtein, E. Zagaynova, D. Conwell, G. Falk, J. Goldblum, J. Dumot, J. Ponsky, G. Gelikonov, B. Davros, E. Donchenko, and J. Richter, "Optical coherence tomography of the esophagus and proximal stomach in health and disease," *The American journal of gastroenterology*, vol. 96, pp. 2633-9, 2001.
- [86] J. Poneros, S. Brand, and B. Bouma, "Diagnosis of specialized intestinal metaplasia by optical coherence tomography," *Gastroenterology*, vol. 120, pp. 7-12, 2001.
- [87] T. J. Romer, J. M. Fitzmaurice, R. M. Cothren, R. Richards-Kortum, R. Petras, J. Sivak, M. V., and J. R. Kramer, "Laser-induced fluorescence microscopy of normal colon and dysplasia in colonic adenomas: implications for spectroscopic diagnosis," *American Journal of Gastroenterology*, vol. 90, pp. 81-87, 1995.

- [88] T. Vo-Dinh, M. Panjehpour, B. F. Overholt, C. Farris, I. Buckley, F. P., and R. Sneed, "In vivo cancer diagnosis of the esophagus using differential normalized fluorescence (DNF) indices," *Lasers in Surgery and Medicine*, vol. 16, pp. 41-47, 1995.
- [89] G. Bottiroli, A. C. Croce, D. Locatelli, R. Marchesini, E. Pignoli, S. Tomatis, C. Cuzzoni, S. Di Palma, M. Dalfante, and P. Spinelli, "Natural fluorescence of normal and neoplastic human colon: a comprehensive," *Lasers in Surgery and Medicine*, vol. 16, pp. 48-60, 1995.
- [90] M. Panjehpour, B. F. Overholt, J. L. Schmidhammer, C. Farris, and P. F. Buckley, "Laser-induced fluorescence spectroscopy: somewhere over the rainbow," *Gastroenterology (selected summaries)*, vol. 110, pp. 643-645, 1996.
- [91] P. T. T. Wong, R. K. Wong, T. A. Caputo, T. A. Godwin, and B. Rigas, "Infrared spectroscopy of exfoliated human cervical cells: evidence of extensive structural changes during carcinogenesis," *Proceedings of the National Academy of Science*, vol. 88, pp. 10988-10992, 1991.
- [92] R. W. Phillips and R. K. H. Wong, "Barrett's esophagus: natural history, incidence, etiology, and complications," *Gastro. Clinics of North America*, vol. 20, pp. 791-815, 1991.
- [93] A. L. Taylor, "The epithelial heterotopias of the alimentary tract," *J. Pathol. Bacteriol.*, vol. 30, pp. 415-449, 1927.
- [94] M. J. Sarr, S. R. Hamilton, and G. C. Marrone, "Barrett's esophagus: its prevalence and association with adenocarcinoma in patients with symptoms of gastroesophageal reflux," *American Journal of Surgery*, vol. 149, pp. 187-194, 1985.
- [95] A. P. Naef, M. Savary, and L. Ozzello, "Columnar-lined lower esophagus: an acquired lesion with malignant predisposition. Report on 140 cases of Barrett's esophagus with 12 adenocarcinomas," *J. Thorac. Cardiovasc. Surg.*, vol. 70, pp. 826-834, 1975.
- [96] A. J. Cameron, B. J. Ott, and W. S. Payne, "The incidence of adenocarcinoma in columnar-lined (Barrett's) esophagus," *New England Journal of Medicine*, vol. 313, pp. 857-859, 1985.
- [97] P. Rozen, M. Baratz, F. Fefer, and T. Gilat, "Low incidence of significant dysplasia in a successful endoscopic surveillance program of patients with ulcerative colitis," *Gastroenter.*, vol. 108, pp. 1361-1370, 1995.
- [98] A. Axon, "Cansurveillance in ulcerative colitis - letter on article," *Gut*, vol. 35, pp. 801, 1994.
- [99] G. J. Tearney, S. A. Boppart, B. E. Bouma, M. E. Brezinski, N. J. Weissman, J. F. Southern, and J. G. Fujimoto, "Scanning single-mode fiber optic catheter-endoscope for optical coherence tomography," *Optics Letters*, vol. 21, pp. 543-5, 1996.
- [100] M. T. Asaki, C. P. Huang, D. Garvey, J. P. Zhou, H. C. Kapteyn, and M. M. Murnane, "Generation of 11-Fs Pulses from a Self-Mode-Locked Ti-Sapphire Laser," *Optics Letters*, vol. 18, pp. 977-979, 1993.
- [101] C. W. Hillegas, J. X. Tull, D. Goswami, D. Strickland, and W. S. Warren, "Femtosecond Laser-Pulse Shaping by Use of Microsecond Radiofrequency Pulses," *Optics Letters*, vol. 19, pp. 737-739, 1994.

Publications supported by AFOSR Contract No. F49620-01-1-0186

1. C. Chudoba, J.G. Fujimoto, E.P. Ippen, H.A. Haus, U. Morgner, F.X. Kärtner, V. Scheuer, G. Angelow, and T. Tschudi, "All-solid-state Cr:forsterite laser generating 14 fs pulses at 1.3 μm ," *Opt. Lett.* **26**, 292-294, March 2001.
2. R. Ell, U. Morgner, F.X. Kärtner, J.G. Fujimoto, E.P. Ippen, V. Scheuer, G. Angelow, T. Tschudi, M.J. Lederer, A. Boiko, and B. Luther-Davies, "Generation of 5-fs pulses and octave-spanning spectra directly from a Ti:Sapphire laser," *Opt. Lett.* **26**, 373-375, March 2001.
3. W. Drexler, U. Morgner, R.K. Ghanta, F.X. Kärtner, J.S. Schuman, and J.G. Fujimoto, "Ultrahigh-resolution ophthalmic optical coherence tomography," *Nat. Med.* **7**, 502-507, April 2001.
4. S.H. Cho, F.X. Kärtner, U. Morgner, E.P. Ippen, J.G. Fujimoto, J.E. Cunningham, and W.H. Knox, "Generation of 90-nJ pulses with a 4 MHz repetition-rate Kerr-lens mode-locked Ti:Al₂O₃ laser operating with net positive and negative intracavity dispersion," *Opt. Lett.* **26**, 560-562, April 2001.
5. M. Brezinski, K. Saunders, C. Jesser, X. Li, and J. Fujimoto, "Index matching to improve optical coherence tomography imaging through blood," *Circulation*, **103**, 1999-2003, April 2001.
6. I. Hartl, X.D. Li, C. Chudoba, R. Ghanta, T. Ko, J.G. Fujimoto, J.K. Ranka, R.S. Windeler, and A.J. Stentz, "Ultrahigh resolution optical coherence tomography using continuum generation in an air-silica microstructure optical fiber," *Opt. Lett.* **26**, 608-610, May 2001.
7. C. Pitris, K.T. Saunders, J.G. Fujimoto, and M.E. Brezinski, "High-resolution imaging of the middle ear with optical coherence tomography: a feasibility study," *Arch. Otolaryngol. Head Neck Surg.* **127**, 637-642, June 2001.
8. W. Drexler, D. Stamper, C. Jesser, X.D. Li, C. Pitris, K. Saunders, S. Martin, M.B. Lodge, J.G. Fujimoto, and M.E. Brezinski, "Correlation of collagen organization with polarization sensitive imaging of in vitro cartilage: implications for osteoarthritis," *J. Rheumatol.* **28**, 1311-1318, June 2001.
9. S.A. Boppart, J.M. Herrmann, C. Pitris, D.L. Stamper, M.E. Brezinski, and J.G. Fujimoto, "Real-time optical coherence tomography for minimally invasive imaging of prostate ablation," *Comput. Aided Surg.* **6**, 94-103, 2001.
10. X. Li, T.H. Ko, and J.G. Fujimoto, "Intraluminal fiber-optic Doppler imaging catheter for structural and functional optical coherence tomography," *Opt. Lett.* **26**, 1906-1909, December 2001.
11. J.G. Fujimoto, "Optical coherence tomography," (C.R. Acad. Sci. Paris, Serie IV) *Appl. Phys.*, 1099-1111, 2001.
12. J.P. Dunkers, F.R. Phelan, C.G. Zimba, K.M. Flynn, D.P. Sanders, R.C. Peterson, R. S. Parnas, X. Li, and J.G. Fujimoto, "The prediction of permeability for an epoxy/E-glass composite using optical coherence tomographic images," *Polymer Composite* **22**, 803-814, December 2001.

13. Z.Y. Williams, J.S. Schuman, L. Gamell, A. Nemi, E. Hertzmark, J.G. Fujimoto, C. Mattox, J. Simpson, and G. Wollstein, "Optical coherence tomography measurement of nerve fiber layer thickness and the likelihood of a visual field defect," *Am. J. Ophthalmol.* **134**, 538-546, October 2002.
14. N.A. Patel, X. Li, D.L. Stamper, J.G. Fujimoto, and M.E. Brezinski, "Guidance of aortic ablation using optical coherence tomography," *Intl. J. Cardiovasc. Imaging* **18**, 2002.
15. A.M. Kowalewicz, T.R. Schibli, F.X. Kärtner, and J.G. Fujimoto, "Ultralow-threshold Kerr-lens mode-locked Ti:Al₂O₃ lasers," *Opt. Lett.* **27**, 2037, November 2002.
16. S. Demos, M. Staggs, K. Minoshima, and J. Fujimoto, "Characterization of laser induced damage sites in optical components," *Opt. Exp.* **10**, 1444-50, November 2002.
17. V. Guedes, J.S. Schuman, E. Hertzmark, G. Wollstein, A. Correnti, R. Mancini, D. Lederer, S. Voskanian, L. Velazquez, H.M. Pakter, T. Pedut-Kloizman, J.G. Fujimoto, and C. Mattox, "Optical coherence tomography measurement of macular and nerve fiber layer thickness in normal and glaucomatous human eyes," *Ophthalmology* **110**, 177-189, January 2003.
18. P.L. Hsiung, X. Li, C. Chudoba, I. Hartl, T.H. Ko, and J.G. Fujimoto, "High-speed path-length scanning with a multiple-pass cavity cell delay line," *Appl. Opt.* **42**, 640-648, February 2003.
19. S.D. Martin, N.A. Patel, S.B. Adams, Jr., M.J. Roberts, S. Plummer, D.L. Stamper, M.E. Brezinski, and J.G. Fujimoto, "New technology for assessing microstructural components of tendons and ligaments," *Intl. Orthop.* **27**, 184-189, February 2003.
20. N.A. Patel, X. Li, D.L. Stamper, J.G. Fujimoto, and M.E. Brezinski, "Guidance of aortic ablation using optical coherence tomography," *Intl. J. Cardiovasc. Imaging* **19**, 171-178, April 2003.
21. J.S. Schuman, G. Wollstein, T. Farra, E. Hertzmark, A. Aydin, J.G. Fujimoto, and L.A. Paunescu, "Comparison of optic nerve head measurements obtained by optical coherence tomography and confocal scanning laser ophthalmoscopy," *Am. J. Ophthalmol.* **135**, 504-512, April 2003.
22. W. Drexler, H. Sattmann, B. Hermann, T.H. Ko, M. Stur, A. Unterhuber, C. Scholda, O. Findl, M. Wirtitsch, J.G. Fujimoto, and A.F. Fercher, "Enhanced visualization of macular pathology with the use of ultrahigh-resolution optical coherence tomography," *Arch. Ophthalmol.* **121**, 695-706, May 2003.
23. R.P. Prasankumar, Y. Hirakawa, A.M. Kowalewicz Jr., F.X. Kärtner, J.G. Fujimoto, and W.H. Knox, "An extended cavity femtosecond Cr:LiSAF laser pumped by low cost diode lasers," *Opt. Exp.* **11**, 1265-1269, May 2003.
24. T.R. Schibli, J. Kim, O. Kuzucu, J.T. Gopinath, S.N. Tandon, G.S. Petrich, L.A. Kolodziejewski, J.G. Fujimoto, E.P. Ippen, and F.X. Kaertner, "Attosecond active synchronization of passively mode-locked lasers by balanced cross correlation," *Opt. Lett.* **28**, 947-949, June 2003.

25. D.E. Lederer, J.S. Schuman, E. Hertzmark, J. Heltzer, L.J. Velazques, J.G. Fujimoto, and C. Mattox, "Analysis of macular volume in normal and glaucomatous eyes using optical coherence tomography," *Am. J. Ophthalmol.* **135**, 838-843, June 2003.
26. T.R. Schibli, O. Kuzucu, J. Kim, E.P. Ippen, J.G. Fujimoto F.X. Kaertner, V. Scheuer and G. Angelow, "Towards single-cycle laser systems," *IEEE J. Selected Topics Quant. Electron.* **9**, 990-1001, July/August 2003.
27. A. Aydin, G. Wollstein, L.L. Price, J.G. Fujimoto, and J.S. Schuman, "Optical coherence tomography assessment of retinal nerve fiber layer thickness changes after glaucoma surgery," *Ophthalmology* **110**: 1506-1511, August 2003.
28. S. Bourquin, R.P. Prasankumar, F X. Kärtner, J.G. Fujimoto, T. Lasser, and R.P. Salathé, "High-speed femtosecond pump-probe spectroscopy using a smart pixel detector array," *Opt. Lett.* **28**, 1588-1590, September 2003.
29. J.G. Fujimoto, "Optical coherence tomography: Principles and applications," *Rev. of Laser Engin.* **31**, 635-642, October 2003.
30. M.J. Roberts, S.B. Adams, Jr., N.A. Patel, D.L. Stamper, M.S. Westmore, S.D. Martin, J.G. Fujimoto, and M.E. Brezinski, "A new approach for assessing early osteoarthritis in the rat," *Anal. Bioanal. Chem.* **377**, 1003-1006, October 2003.
31. A.D. Aguirre, P. Hsiung, T.H. Ko, I. Hartl, and J.G. Fujimoto, "High-resolution optical coherence microscopy for high-speed, in vivo cellular imaging," *Opt. Lett.* **28**, 2064-2066, November 2003.
32. J.G. Fujimoto, "Optical coherence tomography for ultrahigh resolution in vivo imaging," *Nat. Biotechnol.* **21**, 1361-1367, November 2003.
33. E. Lai, G. Wollstein, L.L. Price, L.A. Paunescu, P.C. Stark, J.G. Fujimoto, and J.S. Schuman, "Optical coherence tomography disc assessment in optic nerves with peripapillary atrophy," *Ophthalmic Surg. Lasers Imaging* **34**, 498-504, November/December 2003.
34. S. Bourquin, A.D. Aguirre, I. Hartl, P. Hsiung, T.H. Ko, and J.G. Fujimoto, "Compact broadband light source for ultrahigh resolution optical coherence tomography imaging using a femtosecond Nd:Glass laser and a nonlinear fiber," *Opt. Exp.* **11**, 3290-3297, December 2003.
35. L. Pantanowitz, P.L. Hsiung, T.H. Ko, K. Schneider, P.R. Herz, J.G. Fujimoto, S. Raza, and J.L. Connolly, "High-resolution imaging of the thyroid gland using optical coherence tomography," *Head and Neck* **26**: 425-434, April 2004.
36. T.H. Ko, D.C. Adler, J.G. Fujimoto, D. Mamedov, V. Prokhorov, V. Shidlovski, and S. Yakubovich, "Ultrahigh resolution optical coherence tomography imaging with broadband superluminescent diode light source," *Optics Exp.*, **12**, 2112-2119, May 2004.
37. M. Wojtkowski, V.J. Srinivasan, T.H. Ko, J.G. Fujimoto, J.S. Duker, and A. Kowalevich, "Ultrahigh-resolution, high-speed, Fourier domain optical coherence tomography and methods for dispersion compensation," *Optics Exp.* **12**, 2402-2422, May 2004.

38. J. Rogowska, N.A. Patel, J.G. Fujimoto, and M.E. Brezinski, "optical coherence tomographic elastography technique for measuring deformation and strain of atherosclerotic tissue," *Heart* **90**, 556-562, May 2004.
39. L.A. Paunescu, J.S. Schuman, L.L. Price, P.C. Stark, S. Beaton, H. Ishikawa, G. Wollstein, and J.G. Fujimoto, "Reproducibility of nerve fiber thickness, macular thickness and optic nerve head measurements using StratusOCT optical coherence tomography," *Invest. Ophthalmol. and Vis. Sci.* **45**, 1716-1724, June 2004.
40. P.C. Wagenblast, T.H. Ko, J.G. Fujimoto, F.X. Kaertner, and U. Morgener, "Ultrahigh-resolution ophthalmic optical coherence tomography with diode-pumped broad-band Cr:LiCAF laser," *Opt. Exp.* **12**, 3257-3263, July 2004.
41. P.R. Herz, Y. Chen, A.D. Aguirre, J.G., Fujimoto, H. Mashimo, J. Schmitt, A. Koski, J. Goodnow, and C. Petersen, "Ultrahigh resolution optical biopsy with endoscopic optical coherence tomography," *Opt. Exp.* **12**, 3532-3542, July 2004.
42. G. Wollstein, J.S. Schuman, L.L. Price, A. Aydin, S.A. Beaton, P.C. Stark, J.G. Fujimoto, and H. Ishikawa, "Optical coherence tomography (OCT) macular and peripapillary retinal nerve fiber layer measurements and automated visual fields," *Am. J. Ophthalmol.* **138**, 218-225, August 2004.
43. J.S. Schuman, T. Pedut-Kloizman, E. Hertzmark, M.R. Hee, L. Pieroth, N. Wang, W. C. Kiernan, J.G. Fujimoto, W. Drexler, and R. Ghanta, "Quantitation of nerve fiber layer thickness loss over time in the glaucomatous monkey model using optical coherence tomography," *Arch. Ophthalmol.*, forthcoming.
44. W.P. Roach, C.P. Cain, C.D. DiCarlo, R. Birngruber, J.G. Fujimoto, and C.A. Toth, "The retinal response of macaca mulatta to picosecond laser pulses of varying energy and spot-size," *J. Biomed. Opt.*, forthcoming.
45. T.H. Ko, J.G. Fujimoto, J.S. Duker, L.A. Paunescu, W. Drexler, C.R. Bauman, C. Mattox, E. Reichel, A.H. Rogers, and J.S. Schuman, "Comparison of ultrahigh and standard optical coherence tomography for imaging macular hole pathology and repair," *Ophthalmology*, forthcoming.
46. A. Chan, J.S. Duker, J.S. Schuman, and J.G. Fujimoto, "Stage zero macular holes: observations by optical coherence tomography," *Ophthalmology*, forthcoming.
47. G. Wollstein, J.S. Schuman, L.L. Price, A. Aydin, P.C. Stark, E. Hertzmark, E. Lai, H. Ishikawa, C. Mattox, J.G. Fujimoto, and L.A. Paunescu, "Optical coherence tomography longitudinal evaluation of retinal nerve fiber layer thickness in glaucoma," *Arch. Ophthalmol.*, forthcoming.
48. P.R. Herz, Y. Chen, A. Aguirre, P. Hsiung, K. Schneider, J.G., Fujimoto, H. Mashimo, J. Schmitt, A. Koski, J. Goodnow, and C. Petersen, "Micro-motor endoscope catheter for in vivo ultrahigh resolution optical coherence tomography," *Opt. Lett.*, forthcoming.
49. N. Nishizawa, Y. Chen, P. Hsiung, E.P. Ippen, and J.G. Fujimoto, "Real-time, ultrahigh resolution optical coherence tomography using an all-fiber femtosecond fiber laser continuum at 1.5 μ m," *Opt. Lett.*, forthcoming.

50. D.C. Adler, T.H. Ko, P.R. Herz, and J.G. Fujimoto, "Optical coherence tomography contrast enhancement using noise insensitive spectroscopic analysis," *Opt. Exp.*, forthcoming.
51. D.C. Adler, T.H. Ko, and J.G. Fujimoto, "Speckle reduction in optical coherence tomography images using a spatially adaptive wavelet filter," *Opt. Lett.*, forthcoming.
52. G. Wollstein, L.A. Paunescu, T.H. Ko, A. Kowalevich, I. Hartl, S. Beaton, H. Ishikawa, C. Mattox, O. Singh, W. Drexler, J.G. Fujimoto, and J.S. Schuman, "Ultrahigh resolution optical coherence tomography in glaucoma," *Ophthalmology*, forthcoming.